Sedimentology (2022) **69**, 2463–2485 doi: 10.1111/sed.12997

Permeability heterogeneity of sandstone intrusion fluid-escape systems, Panoche Hills, California: Implications for sedimentary basins globally

BEN CALLOW*,† , ISMAEL HIMAR FALCON-SUAREZ‡ , JONATHAN M. BULL* , THOMAS M. GERNON* , SEAN RUFFELL*,§ , ANTONIO GRIPPA¶,** and ANDREW HURST¶

**National Oceanography Centre Southampton, School of Ocean and Earth Science, University of Southampton, Southampton, SO14 3ZH, UK (E-mail: ben.callow@ugent.be)*
†Department of Geology, PProGRess/UGCT, Ghent University, Ghent, Belgium
‡National Oceanography Centre, Waterfront Campus, Southampton, SO14 3ZH, UK
§Department of Earth Sciences, Durham University, Durham, DH1 3LE, UK
¶School of Geosciences, University of Aberdeen, Aberdeen, AB24 3FX, UK
***Aker BP ASA, Jåttåvågveien 10, Hinna Park, Stavanger, 4020, Norway*

Associate Editor – Kevin Taylor

ABSTRACT

Natural surface gas seeps provide a significant input of greenhouse gas emissions into the Earth's atmosphere and hydrosphere. The gas flux is controlled by the properties of underlying fluid-escape conduits, which are present within sedimentary basins globally. These conduits permit pressure-driven fluid flow, hydraulically connecting deeper strata with the Earth's surface; however they can only be fully resolved at sub-seismic scale. Here, a novel 'minus cement and matrix permeability' method using three-dimensional X-ray micro-computed tomography imaging enables the improved petrophysical linkage of outcrop and sub-surface data. The methodology is applied to the largest known outcrop of an inactive fluid-escape system, the Panoche Giant Intrusion Complex in Central California, where samples were collected along transects of the 600 to 800 m stratigraphic depth range to constrain porosity and permeability spatial heterogeneity. The presence of silica cement and clay matrix within the intergranular pores of sand intrusions are the primary control of porosity (17 to 27%) and permeability (≤1 to *ca* 500 mD) spatial heterogeneity within the outcrop analogue system. Following the digital removal of clay matrix and silica (opal-CT and quartz) cement derived from the mudstone host strata, the sand intrusions have porosity–permeability ranges of *ca* 30 to 40% and 10^3 to 10^4 mD. These calculations are closely comparable to active sub-surface systems in sedimentary basins. Field observations revealed that, at decreasing depth, the connected sand intrusion network reduces in thickness and becomes carbonate cemented, terminating at carbonate mounds formed from methane escape at the seafloor. A new conceptual model integrates the pore-scale calculations and field-scale observations to highlight the key processes that control sand intrusion permeability, spatially and temporally. The study demonstrates the control of matrix and cement addition on the physical properties of fluid-escape conduits, which has significance for hydrocarbon reservoir characterization and modelling, as well as subsurface CO_2 and energy storage containment assessment.

Keywords Cementation, fluid flow, permeability, seal bypass, sandstone intrusion, X-ray micro-CT.

INTRODUCTION

Onshore and offshore surface gas seeps originating from subsurface geological sources provide a substantial flux of greenhouse gas emissions into the Earth's atmosphere and hydrosphere, which affects global climate. Annual global methane emissions supplied from natural geological sources are quantified as 18 to 63 Mt, with offshore seeps contributing 5 to 10 Mt, with significant uncertainty in the calculations (Etiope *et al.*, 2019; Foschi *et al.*, 2020; Saunois *et al.*, 2020). Understanding gas flux rates from onshore and offshore seeps is needed to more precisely quantify the natural input of greenhouse gases into the atmosphere and hydrosphere (Leifer & Boles, 2005; Greinert *et al.*, 2010; Shakhova *et al.*, 2010). The flux rates are controlled by underlying fluid-escape conduits, seal bypass systems which include connected fault and fracture networks, sandstone intrusions and seep structures, present within sedimentary basins globally (Cartwright *et al.*, 2007; Løseth *et al.*, 2009; Andresen, 2012; Karstens & Berndt, 2015). These seal bypass systems permit cross-stratal pressure-driven focused fluid flow, hydraulically connecting deeper strata with the Earth's surface (Cartwright *et al.*, 2007). In addition, these systems may provide leakage pathways through the overburden, where they are directly overlying prospective reservoirs for subsurface carbon dioxide, energy or waste storage (Karstens *et al.*, 2017). A detailed understanding of the geometry, permeability and composition of seal bypass structures is crucial to improving risk assessments and quantifying subsurface fluid-escape fluxes.

Sand injection complexes are regionally-developed seal bypass features (tens to thousands of square kilometres) that form in the shallow crust in response to short-lived (hours to weeks) periods of supra-lithostatic pore-fluid pressure (Vigorito & Hurst, 2010). They form by the forceful injection of fluidized sand, largely in turbulent flow, into actively propagating hydraulic fractures (Hurst *et al.*, 2011). Once emplaced they form highly connected sandstone intrusion networks, in otherwise low permeability host strata that may enable vertical fluid transference from within the host and deeper strata, towards Earth's surface (Hurst *et al.*, 2003a; Cartwright *et al.*, 2007; Grippa *et al.*, 2019). Sand intrusions may enhance fluid transmissivity perpendicular to bedding, creating high permeability pathways through intrinsically low permeability fine-grained strata (Grippa *et al.*, 2019). Discordance with bedding is a key diagnostic of all sandstone intrusions and at all scales of observation (Hurst *et al.*, 2011). Individual sandstone intrusions are most commonly composite (Huuse *et al.*, 2007; Scott *et al.*, 2009; Satur *et al.*, 2021), and vary in size from kilometre-scale length and tens of metres in thickness to centimetre-scale length and thickness (Fig. 1). Independently of the size and geometry of individual intrusions, they commonly exhibit fine to medium grain-size distributions, which is attributed primarily to preferential entrainment of smaller grains into particle suspension, as well as preferential abrasion of larger grains during sand fluidization (Hurst *et al.*, 2003b; Hurst *et al.*, 2011; Hurst *et al.*, 2021a; Gera *et al.*, 2004). Sandstone intrusions are a form of seal bypass feature; however, they are also widely recognized as prospective hydrocarbon reservoirs (Briedis *et al.*, 2007; Huuse *et al.*, 2007).

Using seismic reflection imaging, sand intrusions become more difficult to detect with increasing discordance to host strata bedding (Huuse *et al.*, 2007; Grippa *et al.*, 2019). Three-dimensional seismic surveys resolve the characteristic discordance of low-angle to bedding intrusions, while thin (<5 to 10 m) and steep (>40° to bedding) intrusions are rarely resolved and commonly undetected by seismic as they are beyond seismic resolution (Huuse *et al.*, 2007; Grippa *et al.*, 2019). Also, constructive and destructive tuning effects caused by varying angles of bedding discordance alter sandstone intrusion apparent thickness and geometry inferred from 3D seismic (Grippa *et al.*, 2019). In addition, borehole data may fail to differentiate between parent depositional units and sandstone intrusions, when they have similar mineralogy (Briedis *et al.*, 2007; Lonergan *et al.*, 2007). Dipmeter or borehole image data can identify discordance between bedding and intrusions with confidence, particularly if some

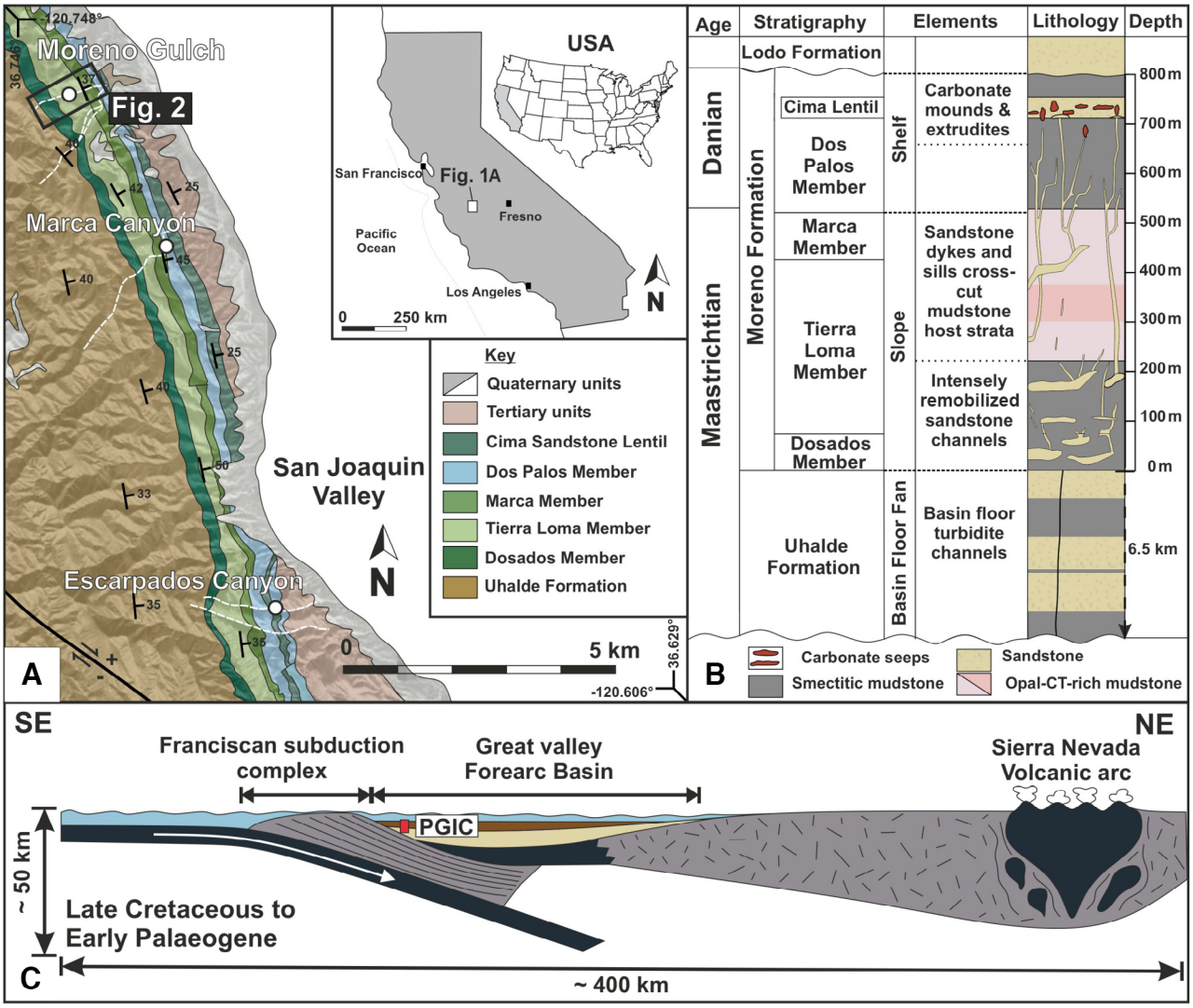

Fig. 1. Regional geological map and stratigraphy of the Panoche Hills field site, central California. (A) Geological map of the Panoche Hills overlaid onto a Google Earth© satellite map. There is a regional 35° north-easterly dip of the rock units towards the San Joaquin Valley. Black box indicates area displayed in Fig. 2. (B) Lithostratigraphic column, for the Panoche Giant Injection Complex (PGIC), a sequence of sand intrusions is present within the Moreno Formation. (C) Simplified diagram (after Ingersoll, 1979) of the Great Valley forearc basin regional tectonics during the Late Cretaceous to Palaeogene. The PGIC is located on the western margin of the Great Valley forearc basin.

drillcore is available for calibration (Duranti *et al.*, 2002; Satur *et al.*, 2021). Detailed study of onshore outcrop analogues has enabled subseismic scale characterization of sand intrusions (e.g. Ross *et al.*, 2014; Cobain *et al.*, 2015).

Petrographic and mineralogical characterization of subsurface sandstone intrusions has received relatively little attention (Duranti *et al.*, 2002) in comparison to outcrop studies (Scott *et al.*, 2009; Bouroullec & Pyles, 2010; Ravier *et al.*, 2015; Zvirtes *et al.*, 2020). Petrographic studies of sandstone intrusions (Duranti & Hurst, 2004; Scott *et al.*, 2009; Hurst *et al.*, 2021a) revealed their (2D) textural immaturity and high content of detrital matrix, relative to depositional parent sandstone. Advances in 3D X-ray micro-computed tomography (μCT) image acquisition systems (Bodey & Rau, 2017), combined with μCT image-processing methods more suitable for analyzing compositionally heterogeneous samples (Callow *et al.*, 2020) provide an opportunity to quantify the physical and textural

properties of heterogeneous sediment samples non-invasively, and with improved accuracy compared to previous preliminary insights (Wu *et al.*, 2017). The μCT method allows *in situ* sample properties to be preserved. In comparison to conventional laboratory methods, μCT does not require invasive sample preparations (for example, thin sections), or the need to modify the original stress state of the sample (for example, flow-through testing) which can induce significant changes to grain fabric of poorly consolidated samples, that directly affect physical property calculations (e.g. Falcon-Suarez *et al.*, 2020).

In this paper, sand intrusion outcrops in the San Joaquin basin, Panoche Hills, Central California (USA) have been characterized. The Panoche Giant Intrusion Complex (PGIC) is the largest known outcrop exposure of sand intrusions on Earth, manifested on a spatial scale of >400 km^2 outcrop exposure and *ca* 1.5 km stratigraphic depth (Fig. 1A to C; Vigorito & Hurst, 2010). Here, a novel three-dimensional μCT image processing and analysis technique is developed to digitally remove pore-filling cement and clay matrix from the intergranular pore volume (IGV) of sandstone intrusion samples. This approach permits the 3D pore-scale investigation of the effect of cement and clay matrix inside the IGV on the porosity and permeability of sandstone intrusions, that previously was limited to 2D analysis (Scott *et al.*, 2013; Ravier *et al.*, 2015). This paper has two main research hypotheses, which form the primary research aims:

1 First, Hurst *et al.* (2021a) revealed the (2D) textural immaturity and high content of detrital matrix in sandstone intrusions of the PGIC, relative to depositional parent sandstones. Therefore, it is hypothesized that the pore-filling detrital clay matrix and cement are the primary control for porosity and permeability at the pore-scale, and therefore account for porosity–permeability spatial heterogeneity at the field-scale within the sandstone PGIC. The hypothesis will be tested using the 'minus cement and matrix' μCT image methodology. Further, detailed petrological analysis of the cement and matrix material, combined with field-scale observations, will also permit a developed understanding of how the cement and matrix formed, and when it was emplaced.

2 Second, it is hypothesized that the processes contributing to the presence of cement and clay matrix, which include mudstone matrix addition and cement growth, are a more site-specific feature of the PGIC outcrop when compared to subsurface analogues. Therefore, the micro-textural observations and physical properties of the outcrop analogue will be compared with previous studies of subsurface sandstone intrusions in the North Sea, such as the Volund Field (Satur *et al.*, 2021) and the Alba Field (Duranti & Hurst, 2004). Given that the PGIC is the most well-recognized outcrop analogue for sandstone intrusions globally (Hurst *et al.*, 2011), which sub-seismic scale sandstone intrusion reservoir models are designed upon, this has major significance.

The pore-scale findings, combined with the field-scale observations, enable the creation of a schematic, conceptual model for the overall geometry, composition and permeability of sandstone intrusion fluid-escape systems, and an assessment of how these properties vary temporally and spatially. This can be used to produce realistic process-based fluid simulation and reactive transport models for hydrocarbon reservoir modelling, or for assessments of fluid leakage through the overburden (Marin-Moreno *et al.*, 2019).

GEOLOGICAL SETTING

The Panoche Hills field outcrop is a type example of a naturally occurring fluid-escape system. The field site is located on the western margin of the San Joaquin Basin in Central California (Fig. 1). The Panoche Hills comprise Mesozoic strata of the Great Valley Group, originally deposited in a forearc basinal setting (Fig. 1; Ingersoll, 1979). This basin was part of a compressive system related to subduction of the Pacific plate, which commenced during the Late Jurassic (Fig. 1; Ingersoll, 2019). Uplift of the Great Valley Basin's western margin commenced in the Quaternary and continues to the present day. The field site has close to 100% exposure and steeply dipping beds (Figs 1 and 2), allowing the fluid-escape system structure, geometry and spatial variability to be constrained.

Marine sediments of the Great Valley Group were deposited from the Late Cretaceous (Cenomanian stage) to the Early Palaeocene (Danian stage) and are unconformably overlain by Late Palaeocene to Middle Eocene sediment (Ingersoll, 1979). The Upper Cretaceous to Early Palaeocene (Danian stage) succession of the

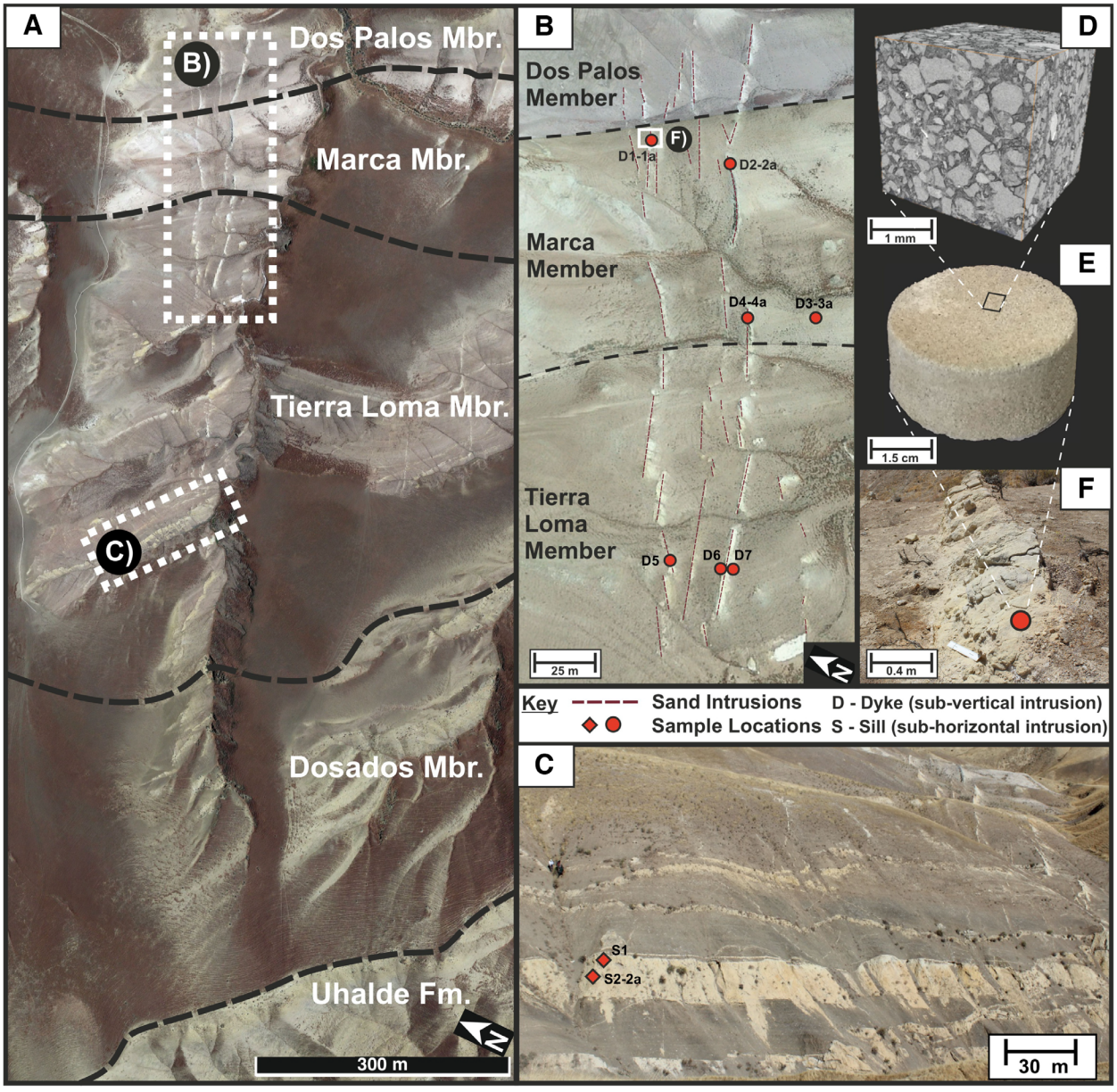

Fig. 2. Sand intrusion sampling locations, collected in Moreno Gulch, Panoche Hills. (A) The Google Earth© satellite map displays the two primary sampling locations within Moreno Gulch: (B) the upper dyke zone and (C) the sill zone. Red circles – sub-vertical sand intrusions – D; Red diamonds – sub-horizontal intrusions – S. (B) The sand intrusion network – dark red dashed lines, is oriented perpendicular to bedding strike direction – black dashed lines. (D) to (F) 5 cm diameter core plugs were sampled (E) and analyzed using 3D X-ray micro-CT imaging (D). Two samples were collected at five locations (for example, 1-1a; Fig. S1 provides additional images of each sampling location).

Panoche Hills comprises two main formations (Fig. 1). Firstly, the top of the Panoche Formation (also termed Uhalde Formation) is composed of interbedded sandstone submarine fan deposits, separated by mudstone intervals (Bartow, 1996). The Moreno Formation conformably overlies the Panoche Formation, representing a transition from a deep marine to shelf setting (Fig. 1B). The Moreno Formation comprises four main members: (i) Dosados Member; (ii) Tierra Loma Member; (iii) Marca Member; and (iv) Dos Palos Member, which contains the sub-unit

Cima Lentil (Fig. 1B; Bartow, 1996; Vigorito *et al.*, 2008).

Emplacement of the PGIC in the early Palaeocene was caused by pore-fluid overpressure in the sandstone-rich lower part of the Moreno Formation exceeding the lithostatic gradient (Vigorito & Hurst, 2010). A period of regional tectonic compression preceded PGIC initiation, but, to date, causal relationships between the regional compression and sand injection have not been established. Intense hydraulic fracturing of overlying mudstone host strata occurred as an immediate precursor to sand injection. Sandstone intrusions in the PGIC have both steep discordance (dykes) and shallow discordance (sills) to bedding; dykes have a near perpendicular orientation to bedding (Vigorito & Hurst, 2010). Sandstone in the PGIC is a hydraulically-connected system, comprising a lower dyke zone, sill zone and upper dyke zone (Fig. 2; Vigorito *et al.*, 2008; Vigorito & Hurst, 2010). Injected sand acted as a fracture proppant, creating permanent fluid-escape pathways that extended through hundreds of metres of overburden and, in some cases, they reached the palaeo-seafloor (Minisini & Schwartz, 2007; Vigorito *et al.*, 2008).

Sand extrudites and methane-derived authigenic carbonates (MDACs) within the Cima Lentil Member are the shallowest stratigraphic level associated with the PGIC (Vigorito *et al.*, 2008; Vigorito & Hurst, 2010). MDACs are present at active seabed methane ebullition sites (Judd & Hovland, 2009). Dating of the carbonates (MDACs) therefore constrains the timing of sand injection to 66 Ma (66 to 62 Ma; Danian; Minisini & Schwartz, 2007; Blouet *et al.*, 2017) and indicates that seabed gas seeps remained active for *ca* 2 Ma (Minisini & Schwartz, 2007).

MATERIALS AND METHODS

Rock samples

Fieldwork was conducted in Moreno Gulch, Marca Canyon and Escarpados Canyon (Fig. 3), across a 600 to 800 m vertical stratigraphic succession of the Moreno Formation (Figs 2 and S1). Moreno Gulch was selected as the primary field sample location, because the outcrop exposure permitted sampling across the full 600 to 800 m stratigraphic range. Sand intrusion samples were collected from Moreno Gulch, along ridgeline transects parallel to bedding (along strike), at multiple stratigraphic depth intervals (Fig. 2). Along those transects, samples were taken at random locations, to minimize self-selection sampling bias. A total of 15 samples were collected from three selected intervals of the dyke zone (D1 to D7), and one interval of the sill zone (S1 to S2). In five locations, two samples were collected (for example, D1 and D1a), to account for localized (centimetre-scale to metre-scale) heterogeneity. Oriented samples were collected from buried, unweathered surfaces, which were dug out and extracted from below the surface regolith, to minimize the effects of surface weathering processes. Field observations and structural measurements were also recorded, including sandstone intrusion orientation, thickness and spacing (Table S1). In addition, an independent study collected three mudstone host strata samples, from Right Angle Canyon, that are representative of each main host rock member (Tierra Loma, Marca and Dos Palos; Hurst *et al.*, 2021b).

From each sample collected in the field, *ca* 25 mm length, 50 mm diameter core plugs are extracted for porosity and permeability determinations in the laboratory (Callow *et al.*, 2020) and 10 mm diameter plugs for 3D X-ray micro-CT (μCT) image analysis (Figs 2, S1 and S2). Additionally, thin sections (30 μm thickness) were prepared for transmitted light microscopy and scanning electron microscopy (SEM), permitting a detailed assessment of sample texture and composition. SEM imaging was performed with a Carl Zeiss Leo 1450 VP scanning electron microscope (SEM) with an energy dispersive spectrometer (EDX; Carl Zeiss AG, Jena, Germany). The sandstone intrusion and host strata mudstone samples were carbon coated and imaged at a pixel resolution of less than 1.5 μm. The elemental composition of each phase was verified using SEM-EDX analysis. Independent XRD (X-ray diffraction) and XRF (X-ray fluorescence) analyses verified the mineralogy and bulk chemistry of the samples, which is further described in Hurst *et al.* (2021b).

X-ray micro-CT image analysis

Micro-CT image acquisition was conducted using an X-ray synchrotron source (Diamond Light Source, Beamline I13-2, Oxford, UK), using a pink beam in the energy range of 20 to 30 keV. Scans were performed on cylindrical

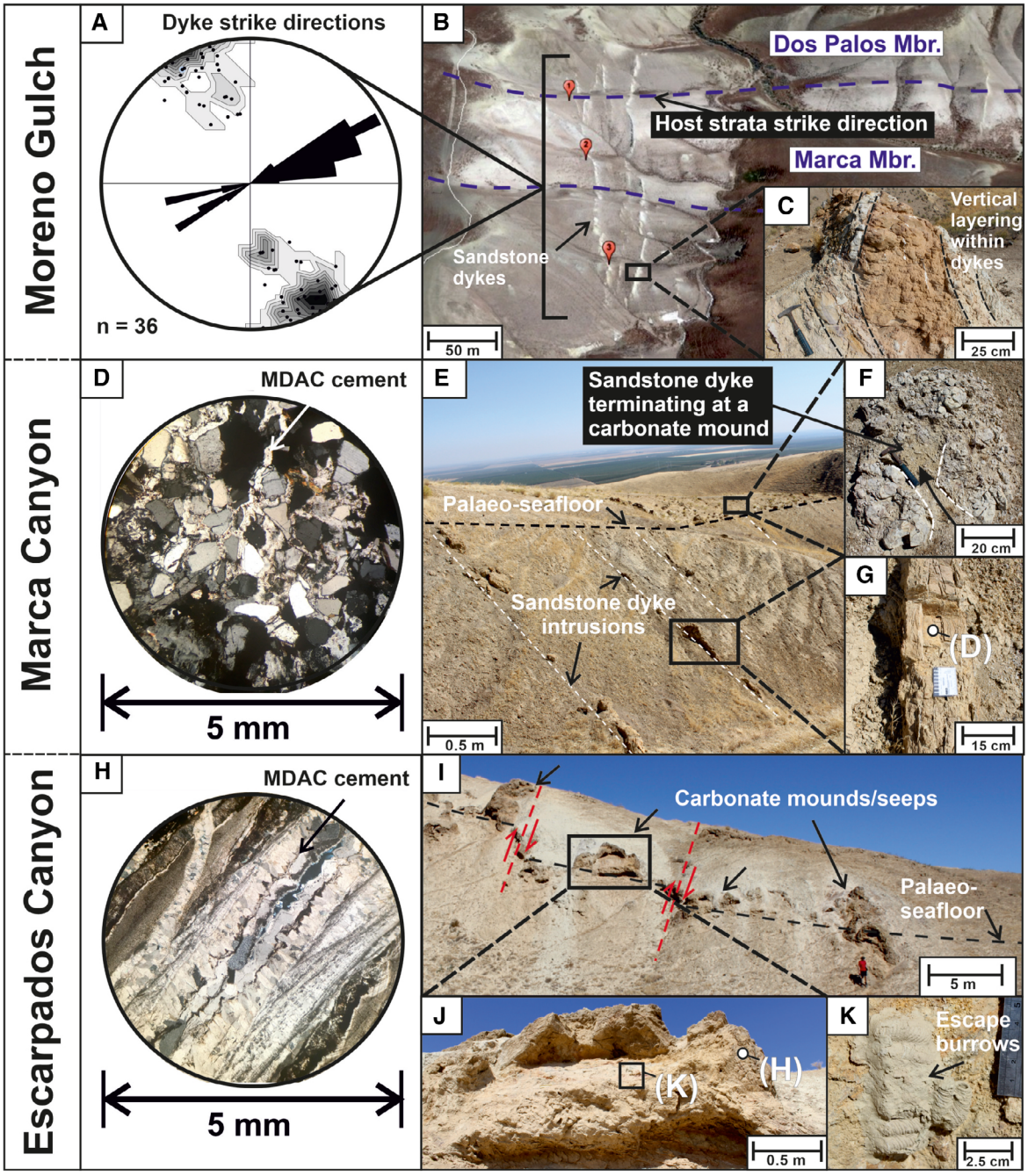

Fig. 3. Photographs highlighting key observations across the sand intrusion system from three main localities of the Panoche Hills field site: Moreno Gulch (A) to (C), Marca Canyon (D) to (G) and Escarpados Canyon (H) to (K). (A) Stereonet showing a modal ENE/WSW dyke orientation trend in Moreno Gulch, which is discordant to the ESE/WNW strike orientation of the host strata bedding (Table S1). (B) View of the upper section of Moreno Gulch, with dykes oriented perpendicular to bedding. (C) Cross-section through a sandstone dyke showing vertical layering, interpreted as multiple pulses of fluidized sediment flow. (D) Thin section of a sandstone dyke, displaying carbonate cementation. (E) Sandstone intrusions terminating at the carbonate mound horizon. (F) Evidence for a sandstone intrusion terminating within a carbonate mound. (G) A carbonate cemented sandstone dyke. (H) Thin section image from a carbonate mound sample, showing carbonate precipitation in discrete layers, which have accreted onto open fracture surfaces. (I) A view of the carbonate mounds which have formed along one main horizon. (J) Closer view of a carbonate mound, showing a sandy core, enveloped by an outer carbonate crust. (K) An escape burrow (fugichnia) present within the sandy core of a carbonate mound. MDAC – methane-derived authigenic carbonate.

samples of 10 mm diameter by 25 mm height and were scanned in dry state (oven-dried at 40°C). The samples were held onto the rotation stage with SEM stubs, which are glued to the sample base. Scans were acquired using a 4× optic and PCO Edge 5.5 scintillator-coupled detector in full frame mode (2560 × 2160 pixels) with a 0.032 magnification, resulting in a pixel resolution of 0.81 μm (Callow *et al.*, 2020). Four thousand equiangular projections were obtained through 360° with a 0.5 s exposure time per projection (25 min per scan; Callow *et al.*, 2020). Image phase contrast is determined by the relative X-ray attenuation of each solid grain and pore-filling phase (Ketcham & Carlson, 2001). A paganin filter (Delta/Beta = 150) was applied to the data during image reconstruction to further enhance the image phase-contrast (Callow *et al.*, 2020). The 32-bit greyscale image volumes produced by the image reconstruction were converted into 8-bit and denoised using a non-local means filter. The high phase contrast images permitted the accurate segmentation and determination of each mineral grain and cement phase [air, quartz, clay matrix and silica cement (opal-CT and quartz), carbonate and iron-oxide] (Fig. S3). Image segmentation was performed using a 3D supervised machine learning technique (Weka) using open-source software (Fig. S3; Arganda-Carreras *et al.*, 2017; Callow *et al.*, 2020). The data were segmented into three classified phases: (1) air; (2) grains; and (3) a combined clay matrix and silica (opal-CT) cement phase (Fig. S3). The air phase (1) corresponds to the intergranular pores resolvable from the μCT image volume, and the grain phase (2) corresponds to the quartz and feldspar grains. The pore-filling clay matrix and silica (opal-CT) cement are estimated to contain 60 to 70% intragranular microporosity, which lies below the μCT image resolution, which is calculated based on mass balance considerations (Callow *et al.*, 2020) and literature microporosity estimates for smectite clay and silica (opal-CT) cement (Hurst & Nadeau, 1995; Alansari *et al.*, 2019).

The μCT image-based analyses were used to quantify the physical properties of each sample, following a workflow outlined in Callow *et al.* (2020; Fig. S2). The calculations acquired included: (i) total and connected (effective) porosity; (ii) pore and grain-size distribution, and (iii) horizontal and vertical absolute permeability.

1 Connected (effective) porosity is defined as voxels assigned to the air phase which are connected by a common face. Total porosity is defined as voxels classified to the air phase combined with 65% of the voxels classified to the combined clay matrix and cement phase, thereby accounting for the intergranular porosity and estimated intragranular microporosity (Fig. S3).

2 Pore and grain-size distributions are calculated by performing a distance transform and watershed transform to the classified air and grain phases of the μCT image volume, respectively (Callow *et al.*, 2020). The transform functions enable the separation and labelling of each pore and grain, which permits the calculation of pore and grain diameter size distribution (Fig. S2). The minimum pore diameter is limited by the 0.81 μm voxel size of the 3D image volumes.

3 Horizontal and vertical absolute permeability simulations determinations are calculated using a Naiver-Stokes finite-element flow solver (Avizo, 2018). The intragranular microporosity of the combined clay and cement phase are assumed to be impermeable, therefore the simulation is applied to the voxels assigned to the connected pore (air) phase.

Further details of the physical property calculations are described in Callow *et al.* (2020).

Callow *et al.* (2020) performed an uncertainty analysis of image resolution, image segmentation, representative elementary volume and finite element volume simulation method for the samples used in this study and determined that the porosity and absolute permeability calculations are accurate to ±1% and within one order of magnitude, respectively. The pore size and absolute permeability were also calculated with the combined clay matrix and cement phase digitally removed. The process of digital removal of the clay matrix and silica (opal-CT) cement (CDR) reclassifies the combined clay matrix and cement phase to the air phase. Thus, the combined effect of cementation and clay matrix addition on the pore property calculations could be assessed.

RESULTS

Field observations

Moreno Gulch

The sand intrusions within the Tierra Loma and Marca members of the Moreno Formation are discordant to bedding (dykes; Fig. 3A and B).

The stereonet shows a rose diagram and poles-to-plane of dyke orientation, showing that the dykes are discordant to the ESE/WNW strike of the host rock strata (Fig. 3A). Distinct vertical layers are present within individual intrusions (Fig. 3C). At greater stratigraphic depths within the Tierra Loma Member, 200 m from the top of the stratigraphic unit, sandstone intrusions are concordant to bedding (sills; Fig. 1). The sandstone sills typically have convex upper margins which indicate previous episodes of the erosive, sub-horizontal flow of fluidized sediment.

Marca Canyon

The sand intrusions extend to the top of the Dos Palos Member of the Moreno Formation. At shallower depths within the Moreno Formation, the thickness of the sandstone dykes decreases from metre-scale to centimetre-scale thickness, and they are carbonate cemented (Fig. 3D to G; Table S1). Despite the decreasing intrusion thickness at shallower stratigraphic depths, the sandstone intrusions extend to a palaeo-seafloor, terminating at carbonate mound structures (Fig. 3E to G).

Escarpados Canyon

Within the Cima Sandstone Lentil Member, the carbonate mound structures extend laterally along one main stratigraphic horizon (Fig. 3). The carbonate mounds display a modal orientation of ESE/WNW strike and 40° dip, which is concordant to the host strata bedding orientation (Table S2). Successive layers are present within the carbonates (Fig. 3H). Ichnofabrics provide evidence that the carbonate structures likely formed at the seafloor (Fig. 3K).

Host rock properties

Scanning electron microscopy analyses of the host rocks revealed that grain size increases from older to younger strata, transitioning from clay to silt-sized grains (Fig. 4). Sub-angular to angular quartz grains are matrix-supported (Fig. 4). SEM-EDS and XRD analyses revealed that the host rock samples are composed of silica (opal-CT and quartz) and smectite clay (Table 1). Smectite comprises *ca* 90% of the phyllosilicate components, with minor illite and kaolinite. Silica is enriched in the two deeper host rock members, comprising *ca* 80% of the non-phyllosilicate components (Table 1). Moulds of diatom test fragments are common, which explains the silica enrichment of the sample matrix (Fig. 4).

X-ray diffraction analysis also shows the relative proportions of the silica mineral phases (Table 1). The opal-CT increases with depth, by up to 17% of the total sample volume. Conversely, opal-A was not detected in any sample (Table 1). SEM imaging reveals 3 to 20 μm sized blade-like crystals that form sub-spherical features, present on relic diatom microfossil tests (Fig. 4).

Sandstone intrusion properties

Grain size

Textural properties of sand intrusion have been evaluated using 3D μCT image data and transmitted light microscopy (Fig. 5). The samples are primarily composed of sub-angular to angular quartz grains. The mean grain sizes are comparable between the sill and dyke samples (*ca* 140 μm), with the former having a greater proportion of grains ≥300 μm diameter (Fig. 5). Hence, the sill samples are poorly sorted, relative to the moderately sorted dyke samples. Grain micro-fracturing is present in the dyke samples, in contrast to the sill samples (Figs 5 and S7). All sample grain-size distributions display a positive skewness (sk > 0.4), due to a high proportion of finer grains relative to the mean (Fig. 5). Petrographic analyses confirm that the pore-filling cement and clay matrix are mostly composed of silica (opal-CT and quartz) and smectite (Fig. 5), which is directly comparable to the mudstone host rock composition (Table 1; Fig. 4). The dyke samples displayed in Fig. 5A and B, represent two end-member samples of high (above 30%), and lower (below 30%) silica (opal-CT) cement and clay matrix volume, respectively. The dyke samples have a higher proportion of pore-filling cement and clay matrix volume (20 to 30%), relative to sill samples (12 to 16%; Table 2; Fig. 5). Overall, dyke samples display a lower textural maturity and a higher proportion of pore-filling silica (opal-CT) cement and smectite clay relative to sill samples.

Porosity–permeability

Sandstone intrusions show connected and total porosity ranges between 1.2 to 18.6% and 16.6 to 26.8%, respectively (Table 2). Sills have a higher connected porosity on average (16.4%) relative to the dykes (8.6%), however their total porosities are comparable (23% and 22%; Table 2). For dykes, non-connected (intragranular) pores represent *ca* 60% of the total pore volume, while only 30% on average for sills. This

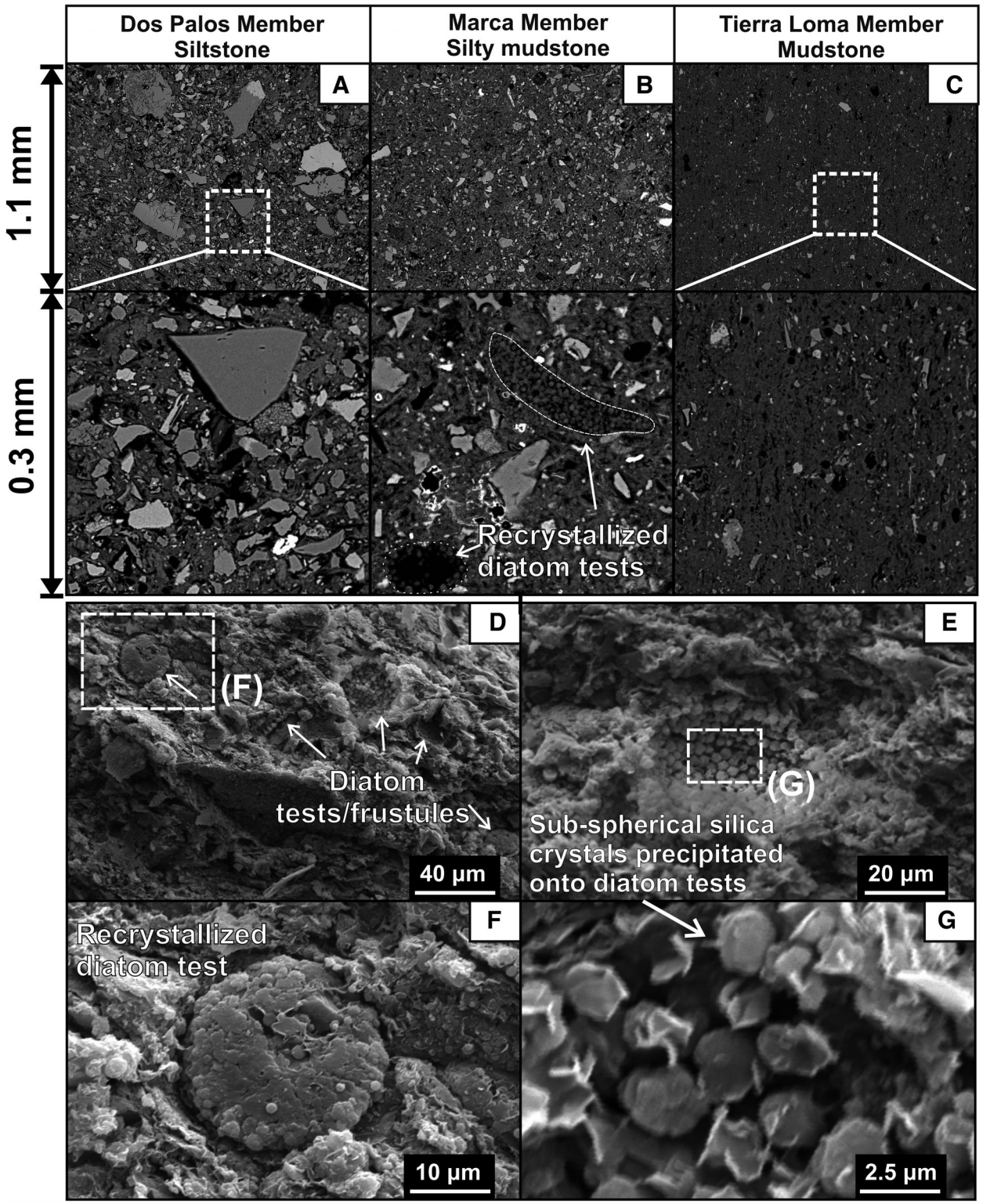

Fig. 4. Scanning electron microscopy images displaying the texture of the fine-grained host strata of the Moreno Formation. (A) Dos Palos Member - siltstone; (B) Marca Member – silty mudstone; (C) Tierra Loma Member – mudstone. SEM-EDX analysis reveals that all samples are siliceous (silica-rich), composed of sub-angular quartz grains in a cement matrix of smectite clay and opal-CT. (D) to (G) Marca Member – evidence of fully recrystallized diatom tests (after Hurst *et al.*, 2021b) highlights a transition from opal-A to opal-CT.

Table 1. X-ray diffraction (XRD) analysis of the host rock mudstones.

	Non-phyllosilicates						Phyllosilicates			
Member	Qtz	Op CT	Op A	Crist	K-feld	Pl	Sm	Ill	Kao	∑Phy
Dos Palos	14.0	0.0	0.0	3.3	4.8	9.2	60.6	2.1	6.0	68.7
Marca	13.4	13.8	0.0	4.5	1.8	5.3	57.5	2.5	1.8	61.8
Tierra Loma	13.1	17.2	0.0	2.2	3.4	6.4	55.4	2.0	0.4	57.8

Qtz = quartz; Op Ct = opal-CT; Op A = opal-A (amorphous silica); Crist = cristobalite; K-feld = K feldspars; Pl = plagioclase feldspar; Sm = smectite; Ill = Illite; Kao = kaolinite; ∑Phy = sum of phyllosilicates. After Hurst *et al.* (2021b).

indicates that a significant proportion of dyke sample pore volume is impermeable. Absolute permeability ranges between *ca* 400 to 500 mD for sills, decreasing by up to two orders of magnitude for dykes (1 to 275 mD). For all samples, the difference between horizontal and vertical permeability is within the error range of the calculations (Fig. 6). Therefore, no significant permeability directional anisotropy is present (Fig. 6).

The sample physical properties were also calculated with the pore-filling silica (opal-CT) cement and clay matrix volume digitally removed (CDR). CDR calculations of porosity and permeability range between 28.1% and 40.8% (average 34%) and 1200 to 6274 mD (average 3120 mD), respectively (Table 2; Figs 6 and S4). CDR permeability calculations represent an increase by up to three orders of magnitude in comparison to the cemented case (≤1 to *ca* 500 mD; Figs 6A, S4 and S5). The increase of sample permeability is directly proportional to the volume of CDR, which indicates that cement and clay matrix are key controlling factors of sand intrusion porosity and permeability.

Pore network modelling

The pore properties of a dyke sample are determined both with and without CDR, using 3D μCT image data (Fig. 7). For the dyke sample without CDR, pore size diameter ranges from <4 to 180 μm, with a 70 μm mean pore size. (Table 2; Fig. 7). There is a bimodal pore size frequency distribution (peaks at 55 μm and 75 μm), with an additional peak below 20 μm, that represents a portion of smaller pores. A comparison of pore size distribution with CDR (Figs 7 and S6), shows that cement and clay matrix infills the modal pore size, indicated by an increased frequency percentage within the 60 to 80 μm range. In addition, the mean pore connectivity of the dykes increases by a factor of two (4.2 to 9.5), as a result of CDR.

DISCUSSION

Insights from the porosity–permeability data

The 3D μCT method combined with more robust image processing workflows (Callow *et al.*, 2020) provide more accurate and non-invasive physical property calculations, in comparison to conventional 2D studies (Scott *et al.*, 2013) and preliminary insights from 3D analyses (Wu *et al.*, 2017). By subtracting specific mineral features from the calculation, their effect on porosity and permeability could be isolated and quantified. This technique has been applied to obtain minus cement and matrix porosity–permeability values, and to determine the horizontal (k_h) and vertical permeability (k_v) components of each sample.

Comparison of sill and dyke sand intrusions

Mean connected porosities of 8.6% for dykes and 16.4% for sills have been calculated. Mean permeability values of 100 mD for high angle dykes and 442 mD for sills have also been calculated. Dyke samples have up to two orders of magnitude lower permeability than sill samples, due to reduced textural maturity (grain microfracturing), as well as increased clay matrix and silica (opal-CT and quartz) cement content (up to 30% of total sample volume; Table 1; Figs 5 and 6). Scott *et al.* (2013) used a large sample set of 2D thin sections to calculate connected porosity values of 5 to 11% for dykes and 12 to 19% for sills, and mean permeability values using a probe permeameter of 81 mD for high angle dykes and 629 mD for sills. These calculations are directly comparable to the results in this study, obtained using the 3D μCT methodology. This highlights that

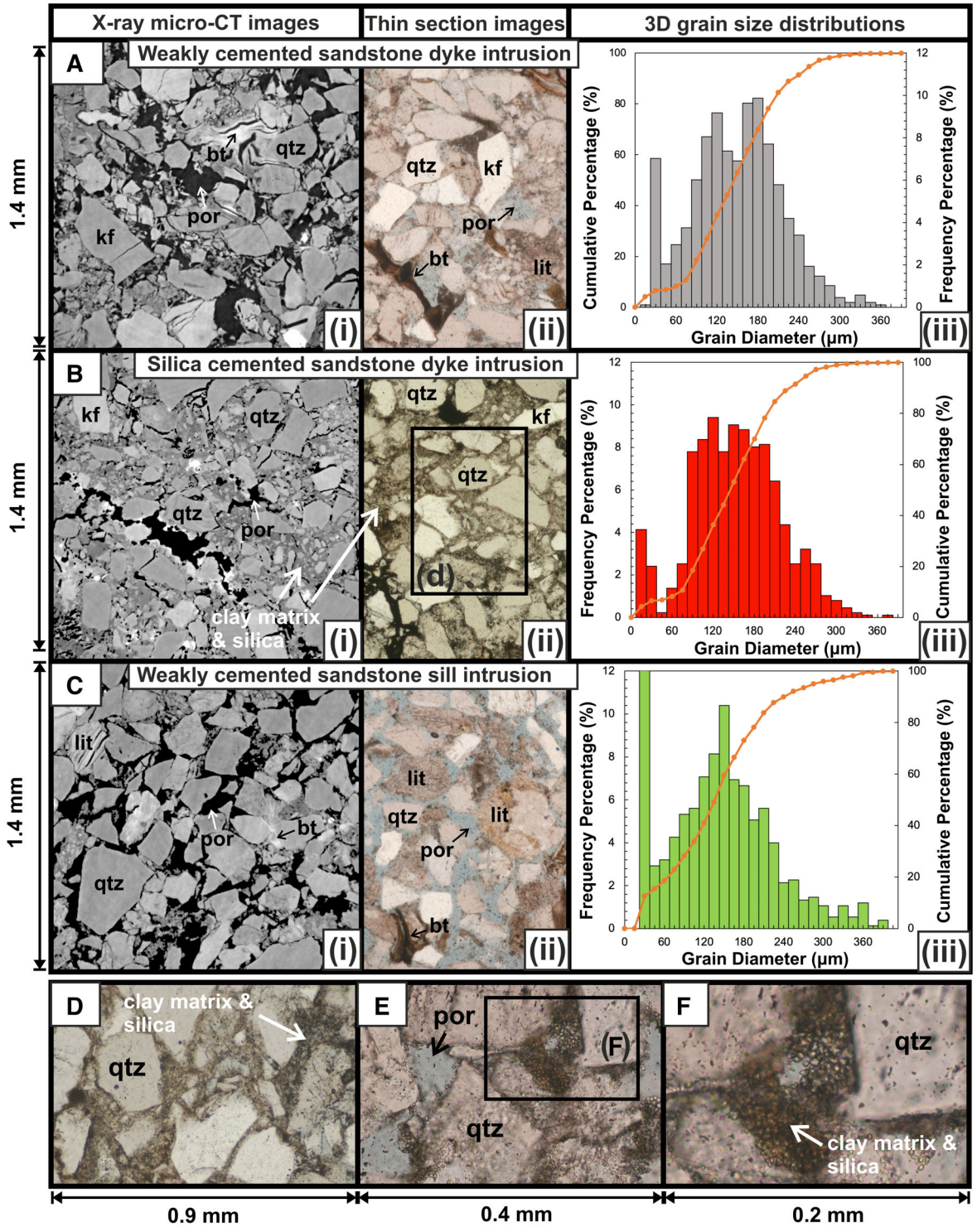

Fig. 5. Two-dimensional images displaying the textural and compositional variability of sandstone intrusions, and their corresponding 3D grain-size distributions. (A) Weakly cemented and (B) cemented sub-vertical intrusions (dykes), as well as (C) a sub-horizontal intrusion (sill). Within (A) to (C): (i) = X-ray micro-CT images, the greyscale reveals areas of low (black) to high (white) X-ray attenuation; (ii) = thin section images using plane polarized light microscopy; (iii) = grain-size distributions derived from 3D X-ray micro-CT image analysis (see Callow *et al.*, 2020, for further details of the methodology). (D) to (F) The clay matrix and cement are composed of a mixture of smectite clay and silica (opal-CT and quartz). qtz – quartz; por – pore space; kf – k-feldspar; bt – biotite mica; lit – lithic grain.

Table 2. Sand intrusion physical properties calculated from X-ray micro-CT image analysis.

Sample	D1	D1a	D2	D2a	D3	D3a	D4	D4a	D5	D6	D7	S1	S2	S2a
Φc (%)	12.9	15.3	1.2	3.5	7.5	6.1	8.9	7.8	8.8	8.3	14.8	13.4	17.1	18.6
Φt (%)	23.6	26.8	18.7	16.6	20.5	20.2	25.2	22.9	21.2	22.1	26.6	21.5	23.4	24.7
Clay/Cement (%)	20.5	22.1	29.8	22.9	23.9	25.5	31.3	28.6	23.1	25.0	22.8	15.7	12.1	11.9
D_D (μm)	69	70	n/a	n/a	67	68	69	68	69	69	69	73	69	70
Av. k (mD)	274	307	≤1	≤1	42	36	73	72	74	52	177	401	388	538
CDR Φt (%)	33.9	37.8	33.7	28.1	32.5	32.9	40.8	37.2	32.8	34.6	38.0	29.4	29.5	30.6
CDR Av. k (mD)	3209	4501	2098	1200	2439	2370	6274	4564	1872	2233	4535	3046	2505	2798

Φc = Connected porosity; Φt = total porosity, where it is assumed/estimated that the clay matrix and cement phases have a microporosity of 50%; Clay/Cement = clay matrix and cement fraction; D_D = Mean pore diameter; Av. k = Mean permeability, an average of vertical (k_v) and horizontal (k_h) permeability; CDR = Clay matrix and cement digitally removed. mD = millidarcies.

intrusions that are more discordant to host strata bedding, which are less discernible from conventional seismic imaging (Grippa *et al.*, 2019), commonly have lower porosity and permeability. This key finding has significance for the assessment and modelling of reservoir volume and fluid containment.

Permeability directional anisotropy

The 3D μCT image analysis enabled assessment of the directional anisotropy of permeability. Calculations of $k_v/k_h > 1$ would indicate enhanced vertical fluid transmissibility. By contrast $k_v/k_h < 1$ would indicate increased permeability concordant to bedding, as displayed by a nearby turbiditic sandstone with pristine depositional structures in the Dosados Member (Wu *et al.*, 2017). In this study, k_v/k_h for sandstone intrusions calculated using μCT imaging are *ca* 1, and within the error of the calculations (Fig. 6B), which suggest very minimal permeability directional anisotropy. The comparison with the depositional sandstone ($k_v/k_h < 1$) supports the interpretation of pervasive grain reorganization due to the action of turbulent flow during sand injection. A previous study of petrographic data from the PGIC was used to determine an average $k_v/k_h = 1.5$ for intrusions in PGIC, which supports the interpretation of grain reorganization and enhanced vertical transmissibility (Scott *et al.*, 2013). Therefore, sand intrusions have a higher vertical permeability relative to depositional sandstones and the surrounding host strata, which highlights their role as sub-vertical fluid-escape structures.

In sandstone intrusions, micro-fractures form by intergranular collisions at high velocity in dilute suspensions (Kleinstreuer, 2010; Hurst *et al.*, 2021a). Using μCT image-based calculations, the minimum fluidization velocity required for sediment entrainment of the PGIC sandstone intrusions (with average grain sizes of 140 μm) is *ca* 0.01 cm/s (Jonk, 2010). Micro-fractured quartz and feldspar grains are characteristic of the studied dyke samples (Figs 5A, 5B and S7) and are analogous to those identified in other sandstone intrusions and extrusions (Scott *et al.*, 2009; Bouroullec & Pyles, 2010). However, the micro-fractures stop at individual grain boundaries and present variable orientation, therefore are unlikely to contribute to permeability anisotropy. Micro-fractures may present variable orientation due to the randomly oriented collisions in a dilute particle suspension during sand injection, as well as further grain reorganization during sediment burial and compaction. Well-developed micro-fractures are also present within nearby Eocene intrusions (>30% micro-fractured grains; Zvirtes *et al.*, 2020).

Insights from the minus cement porosity–permeability data

Comparisons with subsurface field data

The novel minus cement permeability μCT methodology has enabled a closer comparison of outcrop and subsurface data. Clay matrix and silica (opal-CT and quartz) cement have high porosity and low permeability, as they contain a high proportion (60 to 70%) of intragranular (unconnected) pores (Callow *et al.*, 2020). The digital removal of clay matrix and cement (CDR) results in porosity–permeability calculations of 28.1 to 40.8% and 1200 to 6274 mD for the PGIC outcrop sand intrusions (Table 2; Fig. 6). There

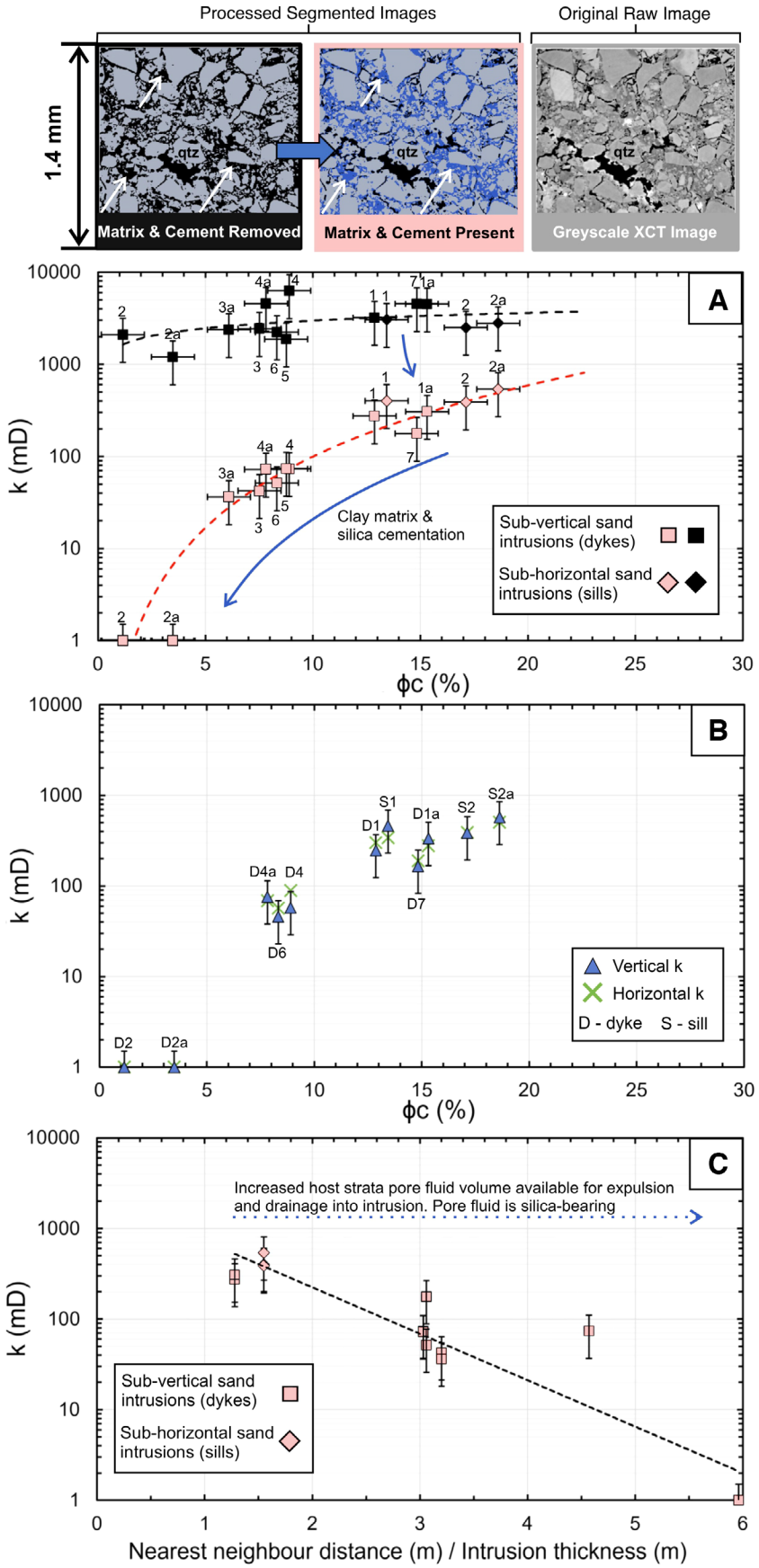

Fig. 6. An assessment of sand intrusion permeability, calculated using μCT image analysis, observing (A) changes caused by cementation, (B) amount of directional anisotropy and (C) correlation to intrusion nearest neighbour distance as a function of thickness. (A) The mean permeability (k) has been calculated for samples D1 to D7 and S1 and S2 with (black) and without (pink) the clay matrix and silica cement digitally removed. The connected porosity (Φc) for all data points (pink and black) is shown for the cemented case, so the permeability reduction is more clearly visible (see Fig. S4 to observe the combined change in porosity–permeability following cement digital removal). Squares – sub-vertical sand intrusions; diamonds – sub-horizontal sand intrusions. (B) Horizontal and vertical permeability (*k*) are compared. Vertical *k* – blue triangles; horizontal *k* – green crosses. The samples display minimal directionally dependent permeability anisotropy. Samples D3 and D5 are omitted as their *in situ* orientation (way-up) is not known. (C) Plot of permeability and distance to nearest neighbour intrusion as a function of intrusion thickness, with exponential correlation (R^2 – 0.86). qtz – quartz.

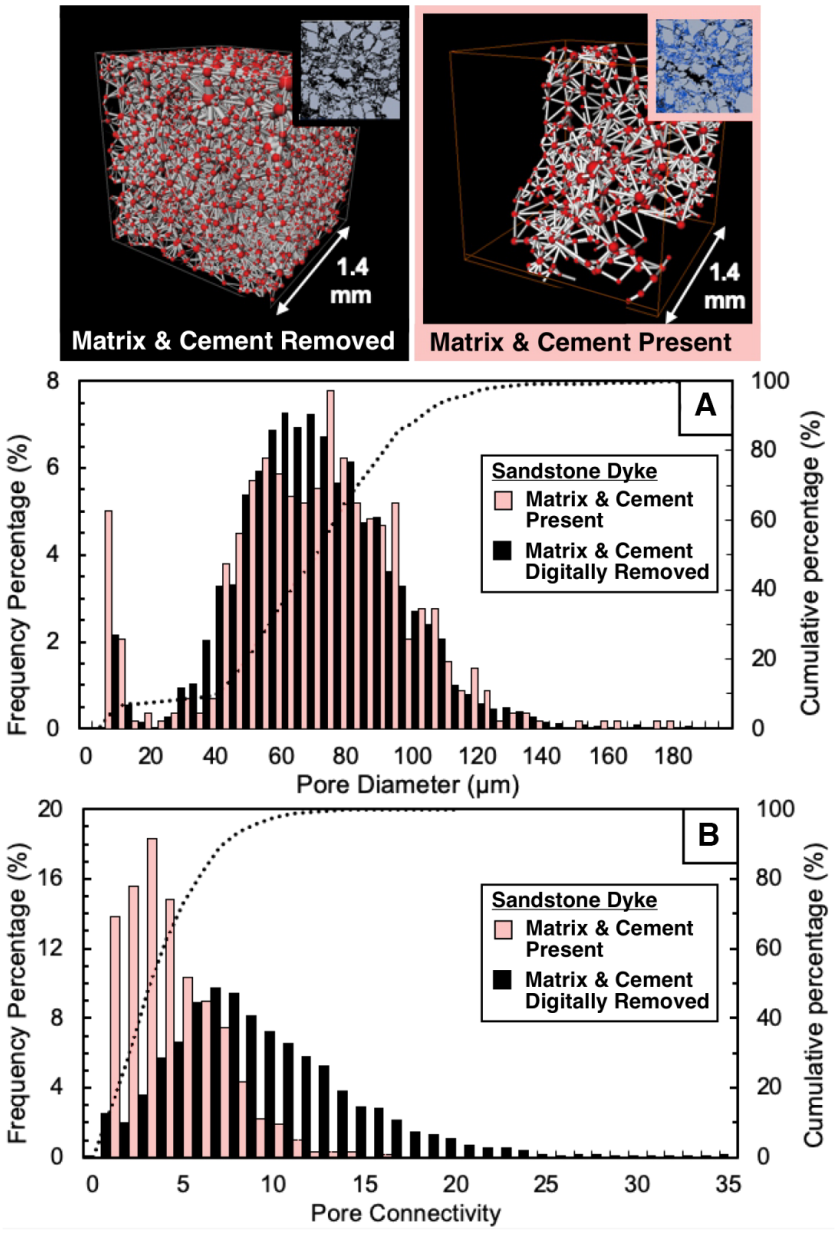

Fig. 7. Pore statistics of a sampled sand intrusion, highlighting the effect of the clay matrix and silica cementation. (A) Frequency percentage histogram of pore diameter. A comparison with (black) and without (pink) the clay matrix and cement digitally removed suggests that cement infills the modal pore size. (B) Frequency percentage histogram of pore connectivity. A comparison suggests that clay matrix and silica cementation causes a significant reduction in pore connectivity. 3D pore network models (PNM) are shown (top and bottom right), derived from the processed 3D X-ray micro-CT images, that were used to obtain the pore statistics. The PNMs display throats/pore connections (grey) and pores (red), on a scale that shows relative pore volume size (scale factor of 3.3E-8) and relative throat equivalent radii (scale factor 0.15).

are limited available porosity and permeability data from subsurface sandstone intrusions. Core data have been used to derive permeability curves for sandstone intrusions in the Volund field, Norwegian North Sea, showing porosity–permeability values of 30 to 40% and 1000 to 8000 mD, respectively (Townsley *et al.*, 2012; Satur *et al.*, 2021). Satur *et al.* (2021) documented no evidence of significant silica cement or silica diagenesis within the Volund Field. Further, Duranti & Hurst (2004) reported a porosity within the range of 30 to 40% and a permeability of 1000 to 10 000 mD for sandstone intrusions in the Alba Field, Witch Ground Graben, North Sea, obtained from 535 (2.5 cm diameter core plugs) samples. Duranti & Hurst (2004) documented a lack of detrital and authigenic clays (usually <2%) within the sandstone intrusions of the Alba Field. Therefore, porosity–permeability measurements from both the Volund and Alba fields are closely comparable to calculations of the PGIC outcrop sand intrusions, after digital removal of clay matrix and silica (opal-CT and quartz) cement volume (CDR; Table 2). Comparable grain sizes, sorting and grain angularity have also been documented

between the sandstone intrusions of the PGIC and the Alba field, which are fine-grained, sub-angular and moderately sorted (Duranti & Hurst, 2004), which further validates the direct comparison of the porosity–permeability calculations.

The PGIC outcrop had an estimated lithostatic gradient of 0.018 MPa m^{-1} and was buried to a maximum depth of 1.5 km (Vigorito & Hurst, 2010), which is comparable to the present-day burial depths and effective stress conditions of the North Sea fields (Hurst *et al.*, 2003a). Sand intrusion formation is a short-lived process of supra-lithostatic pore-fluid pressure (days to weeks; Vigorito & Hurst, 2010). Processes that directly occur after sandstone intrusion formation, such as grain compaction and pore-fluid dewatering, are expected to have occurred for intrusions at both outcrop and subsurface fields. Therefore, mechanical compaction is not considered to be a primary cause for the mismatch between outcrop data (before CDR) and subsurface field data. However, further dewatering will be expected for outcrop data subjected to uplift and exhumation. This may explain the slightly higher permeability ranges present in the Alba Field data (10 000 mD) with respect to the outcrop data (6274 mD). Therefore, significant differences between the physical properties of sandstone intrusions from outcrop analogue data and subsurface field measurements are primarily attributed to intergranular pore-filling clay matrix and cementation of the PGIC.

Clay matrix and silica cementation processes

The proportion of clay matrix and silica (opal-CT and quartz) cement has been interpreted as a unique characteristic feature of the PGIC outcrop data when compared with North Sea subsurface field data. The clay matrix and silica cementation are compositionally identical to that of the surrounding mudstone host strata (Table 1; Hurst *et al.*, 2021b). Therefore, they are interpreted to be sourced from the host strata (Fig. 8). During sand injection and fluidization into hydraulic fractures, erosion of the bio-siliceous mudstone host strata occurs and is reworked by the detachment of angular fragments of the host strata from the margins of fractures during their propagation and filling with fluidized sand (Fig. 8). Spalling of mudstone into fractures continued throughout fluid flow and was likely greatest during the early period of hydraulic fracturing (Zvirtes *et al.*, 2020). Mudstone clasts are present in all samples, and their greater abundance in dyke samples can probably be explained by the increased prevalence of erosional processes for intrusions discordant to bedding (Fig. 5).

Pore network model analysis has here revealed that the silica (opal-CT and quartz) cement infills the modal sized pores of 55 to 75 μm diameter (Fig. 7). Given that the presence of silica and clay matrix appears to be independent of pore size, they are interpreted to have become emplaced during the sandstone intrusion formation, derived from spalls of the host strata that were entrained into the intrusion during formation (Fig. 8). Figure 6C highlighted that, for increased spacing between dykes, a reduction in the permeability of the dykes occurs, which is attributed to the increased percentage of clay matrix and silica in the intergranular pore volume (IGV). This suggests that for more isolated dykes, there is greater entrainment of spalls of host strata into the intrusion. Therefore, if dyke spacing can be quantified from field data, this could improve permeability prediction in sandstone intrusion reservoir models.

Opal-CT, with minor opal-A, is present and locally abundant within the clay mineral rich host strata of the Tierra Loma and Marca members of the Moreno Formation (Table 1; Hurst *et al.*, 2021b) and are present in clasts of the host strata introduced into the sandstone intrusions during their emplacement. Clasts derived from the Marca Member are commonly biosiliceous. Physical evidence of the opal-A to opal-CT transition is preserved as the presence of 3 to 20 μm sub-spherical crystals formed on diatom tests, displayed using SEM image analysis (Fig. 4), and is evidence that opal-A transitions to opal-CT by a dissolution–reprecipitation reaction. In the reaction, intra-crystalline porosity in opal-A decreases with a concomitant increase in opal density as opal-CT forms and mineral-bound water is expelled, an overall volume loss of the solid phase (Isaacs, 1981). Porosity reduction in the diatomaceous component of the matrix of up to 45% is expected during the opal-A to opal-CT conversion (Isaacs, 1981; Weller & Behl, 2015). Porosity reduction in diatomaceous mudstone is a combination of the destruction of commonly <1 μm scale micropores in opal-A, crystal growth of coarser opal-CT with visibly less micropores and mechanical compaction of the coarser opal-CT grains (Fig. 4; Hein *et al.*, 1978; Hurst *et al.*, 2021b). Mudstone from the Tierra Loma and Marca members has generally >12.5% opal-CT (Table 1; Hurst *et al.*,

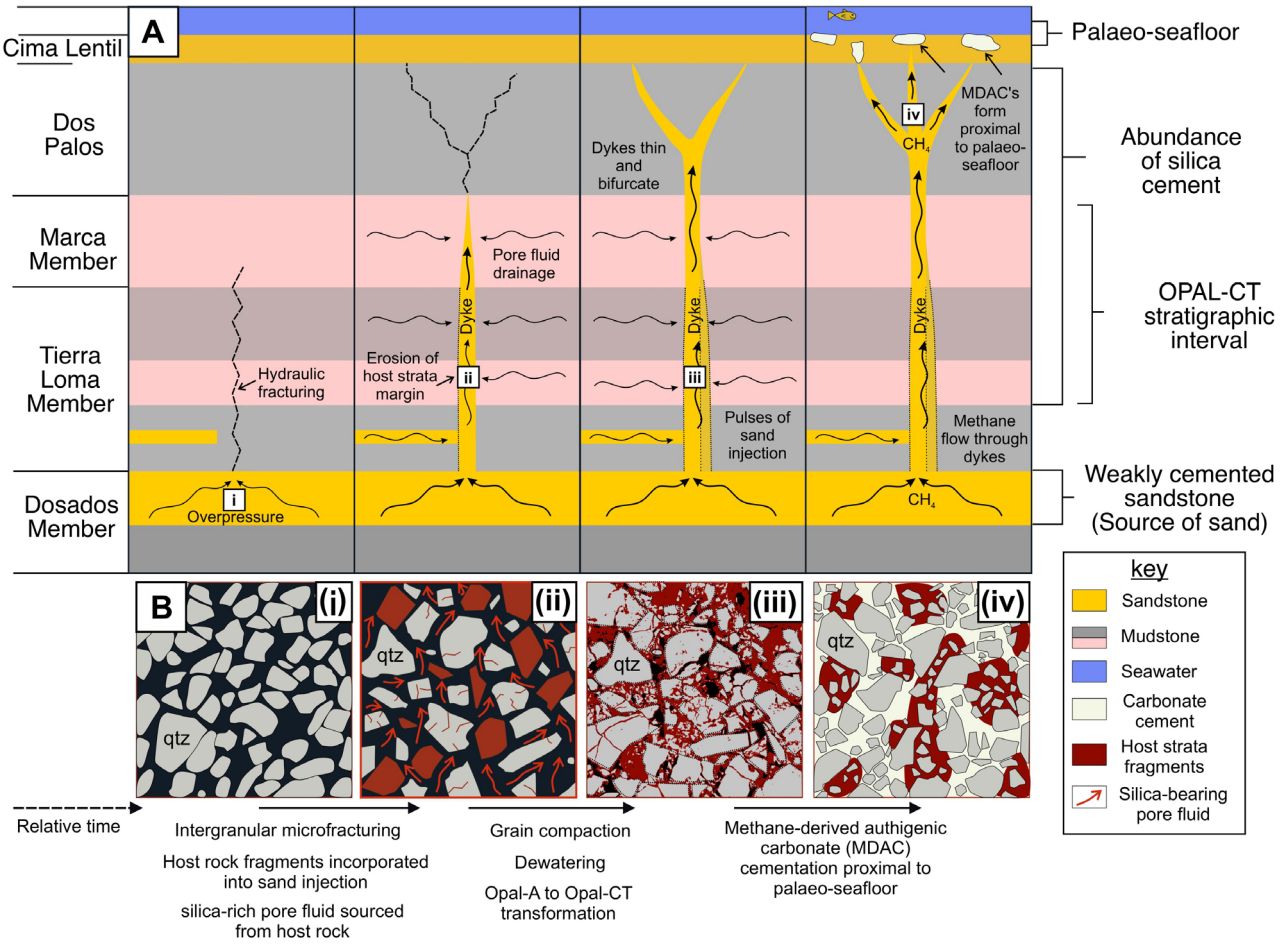

Fig. 8. Conceptual process-based model of a sand intrusion system showing the temporal and spatial evolution of rock texture and pore properties following sand remobilization and intrusion. (A) The temporal development of sand intrusion formation generates a fluid-escape system which extends vertically upward to the seafloor through mudstone host strata. (B) Temporal evolution of rock texture and pore properties (i) to (iv): (i) fluidization and sand remobilization from overpressured parent units; (ii) sand propagates into hydraulic fractures, incorporation of host strata pore waters and erosion-derived clay fragments into the intrusion pore space; (iii) post-fluidization compaction and dewatering of the remobilized sediment; silica transforms from opal-A (amorphous silica) to opal-CT; (iv) methane flows upward through the sand intrusion network; carbonate cementation forms proximal to the seafloor by the process of methane-derived anaerobic oxidation. qtz – quartz.

2021b) so volume reduction is significant where opal-rich clasts are present within the sandstone intrusions (Fig. 5A and B).

Escape of water into the aquifer system during the opal-A to opal-CT transition in biosiliceous mudstone may contribute to sand fluidization and injection, as pore-fluid expulsion can promote fracture generation within host strata by decreasing effective rock strength (Davies *et al.*, 2008). Large-scale sand injectites are present within Cenozoic aged biosiliceous sediments from the North-east Atlantic margin, including the Faeroe–Shetland Basin, the North Viking Graben and the Møre Basin (Davies *et al.*, 2006). Interpretation of seismic surveys from the Faeroe–Shetland Basin reveals seabed pockmarks that overlie probable fluid conduits emanating from intervals with opal-A to opal-CT transition zones (Davies *et al.*, 2006). However, direct evidence is lacking for a genetic relationship between sand injection and the opal-A to opal-CT transition. There is a clear spatial relationship between the PGIC sandstone intrusions and the biosiliceous Marca Member host strata (Fig. 1B). However, all of the sandstone intrusions transect the Marca Member rather than emanate from it. Opal-CT is the dominant silica phase present in the Marca Member (Hurst *et al.*, 2021b), however

the microstructure retains some characteristics of the progenitor diatoms, which indicates that the Marca Member has been lightly consolidated (Fig. 4). This is similar to the moderate dissolution described in SEM images by Hein *et al.* (1978) from Cenozoic deposits, believed to record formation in a temperature range from 35 to 50°C, below a >500 m thick overburden of siliceous ooze. With substantially more data, a study by Varkouhi *et al.* (2021) established a temperature range of <30 to >55°C for the opal-A to opal-CT transition, noting that active silica diagenesis persists at low (<30°C) temperature and gives similar diagenetic products, but more slowly, than a more rapid reaction at higher (>55°C) temperature. Since deposition of the Marca Member (Fig. 1), the SEM analysis suggests that the opal-CT transformation did not reach completion and was predominantly exposed to low temperature, perhaps never much greater than 30°C. Co-occurrence of abundant fully-expandable dioctahedral smectite (Table 1; Hurst *et al.*, 2021b) supports that silicate transformation typically associated with the 60°C isotherm (Nadeau, 2011) was not reached, which is supported by previous observations of preserved epidote and calcic amphibole, heavy minerals typically associated with dissolution during early diagenesis (Hurst *et al.*, 2017). Although the effects of volume reduction and textural change in opal-CT rich clasts in sandstone intrusions are observed (Figs 4 and 5), there is no evidence that opal-A to opal-CT reactions in the host mudstone contributed significant water to sand fluidization and injection. Therefore, sandstone intrusion formation most likely pre-dated the onset of the opal transition.

Permeability distribution

Integration of the field and μCT data permits an improved understanding of sand intrusion formation processes and temporal evolution. Thinning and bifurcation of dykes upward occurs in the PGIC (Fig. 3; Vigorito *et al.*, 2008; Vétel & Cartwright, 2010; Vigorito & Hurst, 2010; Grippa *et al.*, 2019) and in the adjacent Eocene Tumey Giant Injection Complex (Zvirtes *et al.*, 2020). A general reduction in fluid transmissivity is inferred upward in giant injection complexes but, despite this, fluid migration through PGIC dykes caused fluid leakage onto the palaeo-seafloor for *ca* 2 Ma, as evidenced by the presence of MDACs and sandstone extrusions (Minisini & Schwartz, 2007; Blouet *et al.*, 2017). Outcrop observations of individual dykes show subvertical sediment layering and variations in lithification between the sediment layers (*Sandstone intrusion properties* section). Onlapping of the internal layers, crudely from north to south, reveals less consolidation of individual dykes towards their southern margins. A higher permeability was calculated on the southern side of a dyke D7 (177 mD), relative to its northern side D6 (52 mD; Figs 2A and 3C). Southward fracture opening is implied and subsequent filling by later pulses of injected sand (Figs 2, 3 and 8).

Below the Marca Member dykes are commonly >0.5 m across (aperture; Figs 2 to 3) but thin upward in shallower stratigraphic levels (Vigorito *et al.*, 2008; Table S1). Approaching the palaeo-seafloor in the Dos Palos Member (Fig. 2), dykes thin and are prone to carbonate cementation (Figs 3D to G and 8), which in combination reduce their permeability. Böttner *et al.* (2021) observed a permeability reduction in sandstone of three orders of magnitude due to carbonate cementation. Pore-filling carbonate cement forms due to the anaerobic oxidation of methane, a process limited to shallow stratigraphic depths; carbonate cement fills pore throats, preventing advective flow upward (Fig. 8). This process occurred above a subsurface sandstone intrusion system in the Gryphon Field, North Sea (Mazzini *et al.*, 2003).

These observations highlight the reported conclusion that sandstone dykes not only become less permeable as they thin (Scott *et al.*, 2013), but when layers are present, permeability may vary spatially within them. When considering permeability and networks of sandstone dykes, it is inappropriate to assume homogeneous reservoir quality. In quantitative models of mudstone-dominated seal lithologies, where dykes are present and detected on seismic surveys, they are associated with a higher probability of seal failure (Cartwright *et al.*, 2007). If present, but unresolved, on seismic data, this could have detrimental effects on the prediction of seal effectiveness (Grippa *et al.*, 2019). By integrating pore-scale calculations and field-scale observations, input is provided for a conceptual model that assesses a sand intrusion network's influence on seal effectiveness.

Sand intrusion conceptual model

Integrating the pore-scale to field-scale observations, a generally applicable model has been developed for sand intrusion formation, and

process mechanisms that control sand intrusion permeability, spatially and temporally (Fig. 8):

1 Fluidization and sand remobilization from the overpressured parent unit.

2 Sand propagation into hydraulic fractures, erosion (corrasion) of the fine-grained host strata occurs at the fracture margins; fragments and angular spalls of smectite clay and silica are incorporated into the intrusion and incursion of pore waters occurs from the host strata into the intergranular pore space of the sand intrusion.

3 Post-fluidization compaction and dewatering of the remobilized sediment, and silica transformation from opal-A (amorphous silica) to opal-CT due to increased pressure–temperature conditions during burial diagenesis. The opal-A to opal-CT transition occurs after the sand intrusion formation, when the whole succession is becoming more deeply buried.

4 Methane flows upward through the sand intrusion network, resulting in pore-filling carbonate cementation forming proximal to the palaeo-seafloor by the process of methane-derived anaerobic oxidation.

Overall, the main difference between the Panoche Hills with respect to the sand intrusion structures in the North Sea and other sedimentary basins worldwide is the proportion of clay matrix and silica (opal-CT and quartz) cement. In the analysis, when the cement is digitally removed from the IGV using a novel μCT method approach, porosity−permeability values are closely comparable to those reported for North Sea sand intrusions. This observation supports the validity of the proposed conceptual model to explain fluid-escape systems, both spatially and temporally. Evidence from field observations within Moreno Gulch, Marca Canyon and Escarpados Canyon, suggests that the Panoche Hills represents an ancient fluid-escape system from depth to the palaeo-seabed. The cross-stratal fluid flow within the Panoche Hills extends over a stratigraphic thickness of >600 m, which is a comparable vertical scale to observations made within sedimentary basins globally, with sediment remobilization occurring at depth and seep-structures in the near-surface (Fig. 8). Future work should focus on using the findings of the study as a basis for improved process-based fluid simulation and reactive transport models, to understand temporal changes in fluid flux and leakage rates through the sedimentary overburden (Marin-Moreno *et al.*, 2019).

CONCLUSIONS

This study used a novel 'minus cement and matrix' 3D X-ray micro-CT methodological approach to determine pore-scale to field-scale permeability heterogeneity of an ancient fluid-escape system, in the Panoche Hills, California. Overall, the study has provided an improved understanding of the controlling mechanisms of permeability heterogeneity and temporal evolution. The main findings of the study are:

1 The Panoche Hills is an exemplar outcrop analogue of a subsurface fluid-escape system, with comparable spatial scales to active systems in offshore, marine sedimentary basins.

2 The presence of silica (opal-CT and quartz) cement and clay matrix within the intergranular pores of sandstone intrusions are the primary control of porosity and permeability spatial heterogeneity (≤1 to *ca* 500 mD) within the Panoche Giant Injection Complex (PGIC) outcrop analogue system. The digital removal of clay matrix and silica cement results in more directly comparable calculations to modern, offshore systems (i.e. *ca* 30 to 40% porosity and 10^3 to 10^4 mD permeability; Fig. 6).

3 Integration of field-scale to pore-scale observations permits the creation of an improved conceptual geological model that constrains fluid-escape system formation processes and temporal evolution (Fig. 8).

4 Overall, the 3D X-ray micro-CT methodology provides improved quantitative comparisons of outcrop analogues with active, offshore systems. This has future application and broad significance for studies of siliciclastic sediments and fluid-escape systems in sedimentary basins, which has implications for hydrocarbon reservoir characterization, and safe and permanent subsurface carbon storage.

ACKNOWLEDGEMENTS

This work has received funding from the European Union's Horizon 2020 research and innovation programme under grant agreement No. 654462 (STEMM-CCS) and the Natural Environment Research Council (CHIMNEY; NE/N016130/1). We also thank the California Bureau of Land Management for facilitating access to the outcrop area. We acknowledge Diamond Light Source (Beamline I13-2; MT18758). We thank Sharif Ahmed, Hans Deyhle, Hector Marin-Moreno, Laurence North,

Christina Reinhard, Shashi Marathe, Kaz Wanelik, Andrew Bodey, Matthew Beverley-Smith, Daniel Doran, Richard Pearce and the Diamond Support Scientists at I13-2 for their support. We acknowledge the use of the IRIDIS High Performance Computing Facility, μ-VIS X-Ray Imaging Centre, and the SEM facility at the University of Southampton. We acknowledge and thank the British Ocean Sediment Core Research Facility (BOSCORF). We also thank the FEI Visualization Sciences Group for providing the use of the Avizo 9.3.0 software for μCT image processing. Finally, we would like to sincerely thank Richard H. Worden and Thomas Seers for their constructive comments, which greatly improved the manuscript. The data set associated with this work is available online at https://doi.org/10.5258/SOTON/D1441. Here we provide the raw and segmented μCT tomographic image data, and the associated image processing files.

CONFLICT OF INTEREST

The authors declare that they have no known competing financial interests or personal relationships that could have appeared to influence the work reported in this paper.

AUTHOR CONTRIBUTIONS

BC, JMB, TG: Conceptualization. BC, IFS, SR: Formal Analysis. BC, AG, AH, IFS: Validation. BC: Data curation, Methodology, Software, Visualization. BC, JMB: Funding acquisition. BC, AG, AH, IFS, JMB, SR, TG: Investigation & Writing.

DATA AVAILABILITY STATEMENT

The data set associated with this work is available online at https://doi.org/10.5258/SOTON/D1441. Here we provide the raw and segmented μCT tomographic image data, and the associated image processing files.

REFERENCES

Alansari, A., **Salim, A.M.A.**, **Janjuhah, H.T.**, **Bin Abd Rahman, A.H.** and **Fello, N.M.** (2019) Quantification of clay mineral microporosity and its application to water saturation and effective porosity estimation: a case study from Upper Ordovician reservoir, Libya. *J. Nat. Gas Geo.*, **4**, 139–150.

Andresen, K.J. (2012) Fluid flow features in hydrocarbon plumbing systems: what do they tell us about the basin evolution? *Mar. Geol.*, **332**, 89–108. https://doi.org/10.1016/j.margeo.2012.07.006

Arganda-Carreras, I., **Kaynig, V.**, **Rueden, C.**, **Eliceiri, K.W.**, **Schindelin, J.**, **Cardona, A.** and **Seung, H.S.** (2017) Trainable Weka segmentation: a machine learning tool for microscopy pixel classification. *Bioinformatics*, **33**, 2424–2426.

Avizo. (2018). Avizo 3D Software User's Guide. FEI. https://www.fei.com/software/avizo-user-guide/ (accessed 02.10.2019).

Bartow, J.A. (1996) Geologic map of the west border of the San Joaquin Valley in the Panoche Creek-Cantua Creek area, Fresno and San Benito counties, California. US Geological Survey Miscellaneous Geologic Investigations Map I-2430.

Blouet, J.P., **Imbert, P.** and **Foubert, A.** (2017) Mechanisms of biogenic gas migration revealed by seep carbonate paragenesis, Panoche Hills, California. *AAPG Bull.*, **101**, 1309–1340. https://doi.org/10.1306/10171616021

Bodey, A.J. and **Rau, C.** (2017) Launch of the I13–2 data beamline at the Diamond Light Source synchrotron. *J. Phys. Conf. Ser.*, **849**, 012038. https://doi.org/10.1088/1742-6596/849/1/012038

Böttner, C., **Callow, B.J.**, **Schramm, B.**, **Gross, F.**, **Geersen, J.**, **Schmidt, M.**, **Vasilev, A.**, **Petsinski, P.** and **Berndt, C.** (2021) Focused methane migration formed pipe structures in permeable sandstones: insights from uncrewed aerial vehicle-based digital outcrop analysis in Varna, Bulgaria. *Sedimentology*, **68**, 2765–2782. https://doi.org/10.1111/sed.12871

Bouroullec, R. and **Pyles, D.R.** (2010) Sandstone extrusions and slope channel architecture and evolution: Mio-Pliocene Monterey and Capistrano Formations, Dana Point Harbor, Orange County, California, USA. *J. Sediment. Res.*, **80**, 376–392. https://doi.org/10.2110/jsr.2010.043.j

Briedis, N.A., **Bergslien, D.**, **Hjellbakk, A.**, **Hill, R.E.** and **Moir, G.J.** (2007) Recognition Criteria, Significance to Field Performance, and Reservoir Modeling of Sand Injections in the Balder Field, North Sea. In: *Sand Injectites: Implications for Hydrocarbon Exploration and Production* (Eds Hurst, A. and Cartwright, J.), AAPG Memoir, **87**, 91–102.

Callow, B., **Falcon-Suarez, I.**, **Marin-Moreno, H.**, **Bull, J.M.** and **Ahmed, S.** (2020) Optimal X-ray micro-CT image based methods for quantification of porosity and permeability in heterogeneous sandstone. *Geophys. J. Int.*, **223**, 1210–1229. https://doi.org/10.1093/gji/ggaa321

Cartwright, J., **Huuse, M.** and **Aplin, A.** (2007) Seal bypass systems. *AAPG Bull.*, **91**, 1141–1166. https://doi.org/10.1306/04090705181

Cobain, S.L., **Peakall, J.** and **Hodgson, D.M.** (2015) Indicators of propagation direction and relative depth in clastic injectites: implications for laminar versus turbulent flow processes. *Geol. Soc. Am. Bull.*, **127**, 1816–1830. https://doi.org/10.1130/B31209.1

Davies, R.J., **Goulty, N.R.** and **Meadows, D.** (2008) Fluid flow due to the advance of basin-scale silica reaction zones. *Geol. Soc. Am. Bull.*, **120**, 195–206. https://doi.org/10.1130/B26099.1

Davies, R.J., **Huuse, M.**, **Hirst, P.**, **Cartwright, J.** and **Yang, Y.** (2006) Giant clastic intrusions primed by silica diagenesis. *Geology*, **34**, 917. https://doi.org/10.1130/G22937A.1

Duranti, D., **Hurst, A.**, **Bell, C.** and **Groves, S.** (2002) Injected and remobilised sands of the Alba Field (UKCS): sedimentary facies characteristics and wireline log responses. *Petrol. Geosci.*, **8**, 99–107. https://doi.org/10.1144/petgeo.8.2.99

Duranti, D. and **Hurst, A.** (2004) Fluidization and injection in the deep-water sandstones of the Eocene Alba Formation (UK North Sea). *Sedimentology*, **51**, 503–529. https://doi.org/10.1111/j.1365-3091.2004.00634

Etiope, G., **Ciotoli, G.**, **Schwietzke, S.** and **Schoell, M.** (2019) Gridded maps of geological methane emissions and their isotopic signature. *Earth Syst. Sci. Data*, **11**, 1–22. https://doi.org/10.5194/essd-11-1-2019

Falcon-Suarez, I.H., **North, L.**, **Callow, B.**, **Bayrakci, G.**, **Bull, J.** and **Best, A.** (2020) Experimental assessment of the stress-sensitivity of combined elastic and electrical anisotropy in shallow reservoir sandstones. *Geophysics*, **85**, MR271–MR283. https://doi.org/10.1190/geo2019-0612.1

Foschi, M., **Cartwright, J.A.**, **MacMinn, C.W.** and **Etiope, G.** (2020) Evidence for massive emission of methane from a deep-water gas field during the Pliocene. *Proc. Natl Acad. Sci.*, **117**, 27869–27876. https://doi.org/10.1073/pnas.2001904117

Gera, D., **Syamlal, M.** and **O'Brien, T.J.** (2004) Hydrodynamics of particle segregation in fluidized beds. *Int. J. Multiph. Flow*, **30**, 419–428. https://doi.org/10.1016/j.ijmultiphaseflow.2004.01.003

Greinert, J., **McGinnis, D.F.**, **Naudts, L.**, **Linke, P.** and **De Batist, M.** (2010) Atmospheric methane flux from bubbling seeps: spatially extrapolated quantification from a Black Sea shelf area. *J. Geophys. Res. Oceans*, **115**, 1–18. https://doi.org/10.1029/2009JC005381

Grippa, A., **Hurst, A.**, **Palladino, G.**, **Iacopini, D.**, **Lecomte, I.** and **Huuse, M.** (2019) Seismic imaging of complex geometry: forward modeling of sandstone intrusions. *Earth Planet. Sci. Lett.*, **513**, 51–63. https://doi.org/10.1016/j.epsl.2019.02.011

Hein, J.R., **Scholl, D.W.**, **Barron, J.A.**, **Jones, M.G.** and **Miller, J.** (1978) Diagenesis of late Cenozoic diatomaceous deposits and formation of the bottom simulating reflector in the southern Bering Sea. *Sedimentology*, **25**, 155–181. https://doi.org/10.1111/j.1365-3091.1978.tb00307.x

Hurst, A., **Cartwright, J.A.**, **Huuse, M.**, **Jonk, R.**, **Schwab, A.M.**, **Duranti, D.** and **Cronin, B.T.** (2003a) Significance of large-scale sand injectites as long-term fluid conduits: evidence from seismic data. *Geofluids*, **3**, 263–274. https://doi.org/10.1046/j.1468-8123.2003.00066.x

Hurst, A., **Cartwright, J.A.** and **Duranti, D.** (2003b) Fluidisation structures in sandstone produced by upward injection through a sealing lithology. In: *Subsurface Sediment Mobilization* (Eds Van Rensbergen, P., Hillis, R.R., Maltman, A.J. and Morley, C.K.), *Geological Society of London Special Publications*, **216**, 123–137. https://doi.org/10.1144/GSL.SP.2003.216.01.09

Hurst, A., **Luzinski, W.**, **Zvirtes, G.**, **Vigorito, M.**, **Scott, A.**, **Morton, A.C.** and **Wu, F.** (2021a) Diagnostic petrographic and mineralogical criteria for identifying sandstone intrusions. In: *Subsurface Sand Remobilization and Injection: Implications for Oil and Gas Exploration and Development* (Eds Silcock, S., Huuse, M., Bowman, M., Hurst, A. and Cobain, S.). *Geological Society of London Special Publications*, **493**, 287–302. https://doi.org/10.1144/SP493-2018-063

Hurst, A., **Morton, A.**, **Scott, A.**, **Vigorito, M.** and **Frei, D.** (2017) Heavy-mineral assemblages in sandstone intrusions: panoche giant injection complex, California, USA. *J. Sediment. Res.*, **87**, 388–405. https://doi.org/10.2110/jsr.2017.22

Hurst, A. and **Nadeau, P.H.** (1995) Clay microporosity in reservoir sandstones—an application of quantitative electron-microscopy in petrophysical evaluation. *AAPG Bull. Am. Assoc. Petrol. Geol.*, **79**, 563–573. https://doi.org/10.1306/8D2B1598-171E-11D7-8645000102C1865D

Hurst, A., **Scott, A.** and **Vigorito, M.** (2011) Physical characteristics of sand injectites. *Earth Sci. Rev.*, **106**, 215–246. https://doi.org/10.1016/j.earscirev.2011.02.004

Hurst, A., **Wilson, M.J.**, **Grippa, A.**, **Wilson, L.**, **Palladino, G.**, **Belviso, C.** and **Cavalcante, F.** (2021b) Provenance and sedimentary context of clay mineralogy in an evolving forearc basin, upper cretaceous-paleogene and Eocene mudstones, San Joaquin Valley, California. *Minerals*, **11**, 71. https://doi.org/10.3390/min11010071

Huuse, M., **Cartwright, J.**, **Hurst, A.** and **Steinsland, N.** (2007) Seismic characterization of large-scale sandstone intrusions. In: *Sand Injectites: Implications for Hydrocarbon Exploration and Production* (Eds Hurst, A. and Cartwright, J.), AAPG Memoir, **87**, 21–35. https://doi.org/10.1306/1209847M873253

Ingersoll, R.V. (1979) Evolution of the Late Cretaceous forearc basin, northern and central California. *Geol. Soc. Am. Bull.*, **90**, 813. https://doi.org/10.1130/0016-7606(1979)90<813:EOTLCF>2.0.CO;2

Ingersoll, R.V. (2019) Subduction-related sedimentary basins of the US Cordillera. In: *The Sedimentary Basins of the United States and Canada* (Ed. Miall, A.D.), 477–510. doi: https://doi.org/10.1016/B978-0-444-63895-3.00011-5

Isaacs, C.M. (1981) Porosity reduction during diagenesis of the Monterey Formation, Santa Barbara coastal area, California. In: *The Monterey Formation and Related Siliceous Rocks of California* (Eds Garrison, R.E. and Douglas, R.G.), *Society of Economic Paleontologists and Mineralogists, Pacific Section,* **15**, 257–271.

Jonk, R. (2010) Sand-rich injectites in the context of short-lived and long-lived fluid flow. *Basin Res.*, **22**, 603–621. https://doi.org/10.1111/j.1365-2117.2010.00471.x

Judd, A. and **Hovland, M.** (2009) *Seabed Fluid Flow: The Impact on Geology, Biology and the Marine Environment*. Cambridge University Press, Cambridge, 475 pp. https://doi.org/10.1017/CBO9780511535918

Karstens, J., **Ahmed, W.**, **Berndt, C.** and **Class, H.** (2017) Focused fluid flow and the sub-seabed storage of CO2: evaluating the leakage potential of seismic chimney structures for the Sleipner CO2 storage operation. *Mar. Pet. Geol.*, **88**, 81–93. https://doi.org/10.1016/j.marpetgeo.2017.08.003

Karstens, J. and **Berndt, C.** (2015) Seismic chimneys in the Southern Viking Graben – implications for palaeo fluid migration and overpressure evolution. *Earth Planet. Sci. Lett.*, **412**, 88–100. https://doi.org/10.1016/j.epsl.2014.12.017

Ketcham, R.A. and **Carlson, W.D.** (2001) Acquisition, optimization and interpretation of X-ray computed tomographic imagery: applications to the geosciences. *Comput. Geosci.*, **27**, 381–400. https://doi.org/10.1016/S0098-3004(00)00116-3

Kleinstreuer, C. (2010) Dilute particle suspensions. In: *Modern Fluid Dynamics. Fluid Mechanics and Its Applications* (Eds Thess, A. and Moreau, R.), vol. **87**, pp. 307–347. Springer, Dordrecht. doi: https://doi.org/10.1007/978-1-4020-8670-0_6

Leifer, I. and **Boles, J.** (2005) Measurement of marine hydrocarbon seep flow through fractured rock and

unconsolidated sediment. *Mar. Pet. Geol.*, **22**, 551–568. https://doi.org/10.1016/j.marpetgeo.2004.10.026

Lonergan, L., **Borlandelli, C.**, **Taylor, A.**, **Quine, M.** and **Flanagan, K.** (2007) The three-dimensional geometry of sandstone injection complexes in the Gryphon Field, United Kingdom North Sea. In: *Sand Injectites: Implications for Hydrocarbon Exploration and Production* (Eds Hurst, A. and Cartwright, J.), *AAPG Memoir*, **87**, 103–112. doi:https://doi.org/10.1306/1209854M873260

Løseth, H., **Gading, M.** and **Wensaas, L.** (2009) Hydrocarbon leakage interpreted on seismic data. *Mar. Pet. Geol.*, **26**, 1304–1319. https://doi.org/10.1016/j.marpetgeo.2008.09.008

Marin-Moreno, H., **Bull, J.M.**, **Matter, J.**, **Sanderson, D.J.** and **Roche, B.** (2019) Reactive transport modelling insights into CO_2 migration through sub-vertical fluid flow structures. *Int. J. Greenhouse Gas Control*, **86**, 82–92. https://doi.org/10.1016/j.ijggc.2019.04.018

Mazzini, A., **Duranti, D.**, **Jonk, R.**, **Parnell, J.**, **Cronin, B.T.**, **Hurst, A.** and **Quine, M.** (2003) Palaeo-carbonate seep structures above an oil reservoir, Gryphon Field, Tertiary, North Sea. *Geo-Mar. Lett.*, **23**, 323–339. https://doi.org/10.1007/s00367-003-0145-y

Minisini, D. and **Schwartz, H.** (2007) An early Paleocene cold seep system in the Panoche and Tumey Hills, central California (United States). In: *Sand Injectites: Implications for Hydrocarbon Exploration and Production* (Eds Hurst, A. and Cartwright, J.), *AAPG Memoir*, **87**, 185–197. doi: https://doi.org/10.1306/1209862M873264

Nadeau, P.H. (2011) Earth's energy "Golden Zone": a synthesis from mineralogical research. *Clay Miner.*, **46**, 1–24. https://doi.org/10.1180/claymin.2011.046.1.1

Ravier, E., **Guiraud, M.**, **Guillien, A.**, **Vennin, E.**, **Buoncristiani, J.-F.** and **Portier, E.** (2015) Micro- to macro-scale internal structures, diagenesis and petrophysical evolution of injectite networks in the Vocontian Basin (France): implications for fluid flow. *Mar. Pet. Geol.*, **64**, 125–151. https://doi.org/10.1016/j.marpetgeo.2015.02.040

Ross, J.A., **Peakall, J.** and **Keevil, G.M.** (2014) Facies and flow regimes of sandstone-hosted columnar intrusions: insights from the pipes of Kodachrome Basin State Park. *Sedimentology*, **61**, 1764–1792. https://doi.org/10.1111/sed.12115

Satur, N., **Hurst, A.**, **Bang, A.**, **Skjærpe, I.** and **Muehlboeck, S.A.** (2021) Characteristics of an injection wing, Volund Field. In: *Subsurface Sand Remobilization and Injection: Implications for Oil and Gas Exploration and Development* (Eds Silcock, S., Huuse, M., Bowman, M., Hurst, A. and Cobain, S.), *Geological Society of London Special Publications*, **493**, 151–166. https://doi.org/10.1144/SP493-2017-309

Saunois, M., **Stavert, A.R.**, **Poulter, B.**, **Bousquet, P.**, **Canadell, J.G.**, **Jackson, R.B.**, **Raymond, P.A.**, **Dlugokencky, E.J.**, **Houweling, S.**, **Patra, P.K.**, **Ciais, P.**, **Arora, V.K.**, **Bastviken, D.**, **Bergamaschi, P.**, **Blake, D.R.**, **Brailsford, G.**, **Bruhwiler, L.**, **Carlson, K.M.**, **Carrol, M.**, **Castaldi, S.**, **Chandra, N.**, **Crevoisier, C.**, **Crill, P.M.**, **Covey, K.**, **Curry, C.L.**, **Etiope, G.**, **Frankenberg, C.**, **Gedney, N.**, **Hegglin, M.I.**, **Höglund-Isaksson, L.**, **Hugelius, G.**, **Ishizawa, M.**, **Ito, A.**, **Janssens-Maenhout, G.**, **Jensen, K.M.**, **Joos, F.**, **Kleinen, T.**, **Krummel, P.B.**, **Langenfelds, R.L.**, **Laruelle, G.G.**, **Liu, L.**, **Machida, T.**, **Maksyutov, S.**, **McDonald, K.C.**, **McNorton, J.**, **Miller, P.A.**, **Melton, J.R.**, **Morino, I.**, **Müller, J.**, **Murguia-Flores, F.**, **Naik, V.**, **Niwa, Y.**, **Noce, S.**, **O'Doherty, S.**, **Parker, R.J.**, **Peng, C.**, **Peng, S.**, **Peters, G.P.**, **Prigent, C.**, **Prinn, R.**, **Ramonet, M.**, **Regnier, P.**, **Riley, W.J.**, **Rosentreter, J.A.**, **Segers, A.**, **Simpson, I.J.**, **Shi, H.**, **Smith, S.J.**, **Steele, L.P.**, **Thornton, B.F.**, **Tian, H.**, **Tohjima, Y.**, **Tubiello, F.N.**, **Tsuruta, A.**, **Viovy, N.**, **Voulgarakis, A.**, **Weber, T.S.**, **van Weele, M.**, **van der Werf, G.R.**, **Weiss, R.F.**, **Worthy, D.**, **Wunch, D.**, **Yin, Y.I.**, **Yoshida, Y.**, **Zhang, W.**, **Zhang, Z.**, **Zhao, Y.**, **Zheng, B.O.**, **Zhu, Q.**, **Zhu, Q.** and **Zhuang, Q.** (2020) The Global Methane Budget 2000–2017. *Earth System Science Data*, **12**, 1561–1623. https://doi.org/10.5194/essd-12-1561-2020

Scott, A., **Hurst, A.** and **Vigorito, M.** (2013) Outcrop-based reservoir characterization of a kilometer-scale sand-injectite complex. *AAPG Bull.*, **97**, 309–343. https://doi.org/10.1306/05141211184

Scott, A., **Vigorito, M.** and **Hurst, A.** (2009) The process of sand injection: internal structures and relationships with host strata (Yellowbank Creek Injectite Complex, California, U.S.A.). *J. Sediment. Res.*, **79**, 568–583. https://doi.org/10.2110/jsr.2009.062

Shakhova, N., **Semiletov, I.**, **Salyuk, A.**, **Yusupov, V.**, **Kosmach, D.** and **Gustafsson, Ö.** (2010) Extensive methane venting to the atmosphere from sediments of the East Siberian Arctic Shelf. *Science*, **327**, 1246–1250. https://doi.org/10.1126/science.1182221

Townsley, A., **Schwab, A.M.** and **Jameson, E.W.** (2012) The Volund Field: developing a unique sand injection complex in Offshore Norway. European Association of Geoscientists & Engineers, Europec, Copenhagen, SPE 154912, doi: https://doi.org/10.2118/154912-MS

Varkouhi, S., **Tosca, N.J.** and **Cartwright, J.A.** (2021) Temperature–time relationships and their implications for thermal history and modelling of silica diagenesis in deep-sea sediments. *Mar. Geol.*, **439**, 106541. https://doi.org/10.1016/j.margeo.2021.106541

Vétel, W. and **Cartwright, J.** (2010) Emplacement mechanics of sandstone intrusions: insights from the Panoche Giant Injection Complex, California. *Basin Res.*, **22**, 783–807. https://doi.org/10.1111/j.1365-2117.2009.00439.x

Vigorito, M., **Hurst, A.**, **Cartwright, J.** and **Scott, A.** (2008) Regional-scale shallow crustal remobilization: processes and architecture. *J. Geol. Soc.*, **165**, 609–612. https://doi.org/10.1144/0016-76492007-096

Vigorito, M. and **Hurst, A.** (2010) Regional sand injectite architecture as a record of pore-pressure evolution and sand redistribution in the shallow crust: insights from the Panoche Giant Injection Complex, California. *J. Geol. Soc.*, **167**, 889–904. https://doi.org/10.1144/0016-76492010-004

Weller, R. and **Behl, R.J.** (2015) Physical and Mechanical Characteristics of the Opal-A to Opal-CT Transition Zone: Enhanced Diatomite Permeability from Heterogeneous Diagenetic Embrittlement: Oxnard, California, Pacific Section of American Association of Petroleum Geologists, Society of Economic Geologists and Society for Sedimentary Geology, Joint Technical Conference, 51112.

Wu, F., **Hurst, A.** and **Grippa, A.** (2017) Grain and pore microtexture in sandstone sill and depositional sandstone reservoirs: preliminary insights. *Petrol. Geosci.*, **24**, 236–243. https://doi.org/10.1144/petgeo2017-027

Zvirtes, G., **Philipp, R.P.**, **Hurst, A.**, **Palladino, G.**, **De Ros, L.F.** and **Grippa, A.** (2020) Petrofacies of Eocene sand injectites of the Tumey Giant Injection Complex, California (USA). *Sed. Geol.*, **400**, 105617. https://doi.org/10.1016/j.sedgeo.2020.105617

Manuscript received 18 May 2021; revision accepted 22 March 2022

Supporting Information

Additional information may be found in the online version of this article:

Figure S1. Sand intrusion sampling locations, collected in Moreno Gulch, Panoche Hills.

Figure S2. A summary of the 3D X-ray micro-CT image processing and analysis used in this study.

Figure S3. Greyscale intensity curves, highlighting the segmentation and distinction of different phases during 3D X-ray micro-CT image processing.

Figure S4. Porosity–permeability plot, highlighting the porosity and permeability reduction caused by clay matrix and silica (Opal-CT and quartz) cementation.

Figure S5. A plot of sand intrusion permeability versus intrusion thickness.

Figure S6. Pore statistics of sampled sand intrusions provides a comparison between a silica cemented dyke (pink) and a sill (grey).

Figure S7. Scanning electron microscopy images displaying the textural and compositional variability of sandstone intrusions.

Table S1. Moreno Gulch and Marca Canyon – Structural Field Measurements of Sandstone Intrusions.

Table S2. Marca Canyon and Escarpados Canyon – Structural Field Measurements of Carbonate Mound.